JGR Solid Earth

RESEARCH ARTICLE
10.1029/2019JB018297

Special Section:
Magnetism in the Geosciences - Advances and Perspectives

Recordings of Fast Paleomagnetic Reversals in a 1.2 Ma Greigite-Rich Sediment Archive From Lake Ohrid, Balkans

J. Just[1], L. Sagnotti[2], N. R. Nowaczyk[3], A. Francke[4], and B. Wagner[5]

[1]Faculty of Geoscience, University of Bremen, Bremen, Germany, [2]Istituto Nazionale di Geofisica e Vulcanologia, Rome, Italy, [3]Helmholtz Centre Potsdam, GFZ German Research Centre for Geosciences, Potsdam, Germany, [4]School of Earth, Atmosphere, and Life Science, University of Wollongong, Wollongong, new South Wales, Australia, [5]Institute of Geology and Mineralogy, University of Cologne, Cologne, Germany

Abstract State-of-the-art paleoclimate research strongly depends on the availability of time-equivalent markers as chronological control to disentangle interrelationships in the climate system from regional to global scale. Geomagnetic reversals are regarded as excellent age constraints because they are global events and independent from climatic conditions. However, spatial variations of timing and internal dynamics of reversals may limit their precision. Our 1.2 Ma high-resolution (~25 cm/kyr) sediment record from Lake Ohrid is promising to precisely depict the Matuyama-Brunhes (MB) reversal and the Jaramillo subchron. Two generations of diagenetic ferrimagnetic minerals are present in glacial intervals of the Lake Ohrid record. Early diagenetic greigite acquired a quasi synsedimentary chemical magnetization, while a late diagenetic greigite formation, triggered by the upward diffusion of H_2S-rich waters, obscures the polarity record at the top of the Jaramillo. Interglacial intervals are unaffected by greigite formation, likely due to low iron concentrations. Based on an orbitally tuned age model with tephrostratigraphic markers, the base of Jaramillo can be precisely dated to 1072.4 ka, and the MB reversal to 778.5 ka. Both polarity reversals occurred very rapidly in our record, lasting 2.3 and 1 kyr, respectively. Our results reveal that the dipole component of the Earth's magnetic field fell below the nondipole components only for a short duration in the Mediterranean region. The comparison of the timing of the MB boundary across different archives implies that the onset of the reversal provides a more synchronous age marker compared to often used midpoint ages.

Key Points:
- Two generations of diagenetic greigite occur in Lake Ohrid sediments but are constrained to glacial intervals
- Paleomagnetic reversal processes took less than 1 kyr for the Matuyama-Brunhes reversal and 2.3 kyr for the base of the Jaramillo subchron
- The onset of the Matuyama-Brunhes reversal is spatially more synchronous than its midpoint and should be used for stratigraphic correlation

Supporting Information:
- Supporting Information S1

Correspondence to:
J. Just,
janna.just@uni-bremen.de

Citation:
Just, J., Sagnotti, L., Nowaczyk, N. R., Francke, A., & Wagner, B. (2019). Recordings of fast paleomagnetic reversals in a 1.2 ma greigite-rich sediment archive from lake ohrid, balkans. *Journal of Geophysical Research: Solid Earth*, *124*, 12,445–12,464. https://doi.org/10.1029/2019JB018297

Received 4 JUL 2019
Accepted 12 NOV 2019
Accepted article online 19 NOV 2019
Published online 21 DEC 2019

©2019. The Authors.
This is an open access article under the terms of the Creative Commons Attribution License, which permits use, distribution and reproduction in any medium, provided the original work is properly cited.

1. Introduction

Geomagnetic reversals are indispensable as chronological markers in sedimentary archives and volcanic rocks, giving age constraints over time intervals of millions of years. In order to provide precise age-equivalent markers, paleomagnetic reversals need to be accurately dated. Especially in state-of-the-art paleoclimatic studies for which leads, lags, and feedbacks between the terrestrial and marine realms and across ocean basins and ice sheets are being investigated, formally constrained ages that fall within intervals of ± a few kyr are not sufficient.

The Matuyama-Brunhes (MB) reversal is the youngest and best studied transition, mainly because representative stratigraphic successions are widespread and easy to access, and paleomagnetic records have not been overprinted repeatedly by a reversing magnetic field. For the global benthic oxygen isotope stack LR04 (Lisiecki & Raymo, 2005) and for the Geomagnetic Polarity Time Scale (GPTS; Ogg, 2012) an age of 782 ka (±4 kyr) is suggested for the MB transition, stratigraphically positioned in Marine Isotope Stage (MIS) 19. The midpoint ages of the MB in different sedimentary archives integrate over 782 to 770 ka (Figure 1). This age range covers a stratigraphic interval from the peak interstadial MIS 19c to the onset of stage MIS 19a, which is a significant difference from a paleoclimatic perspective with implications for stratigraphic correlation. Interestingly, the onset of the MB reversal appears more synchronous for the gross of those records. Volcanic ages are often much older (Figure 1, up to 798 ka) but were discussed to indicate the initial demise of the dipole component (Singer et al., 2005). Even more surprising than the large age range are the markedly different estimates on the durations of the MB transition. The most rapid postulated reversal was evidenced at sites in Italy (Macrì et al., 2018; Sagnotti et al., 2014; Sagnotti et al., 2016) and high-resolution sites from

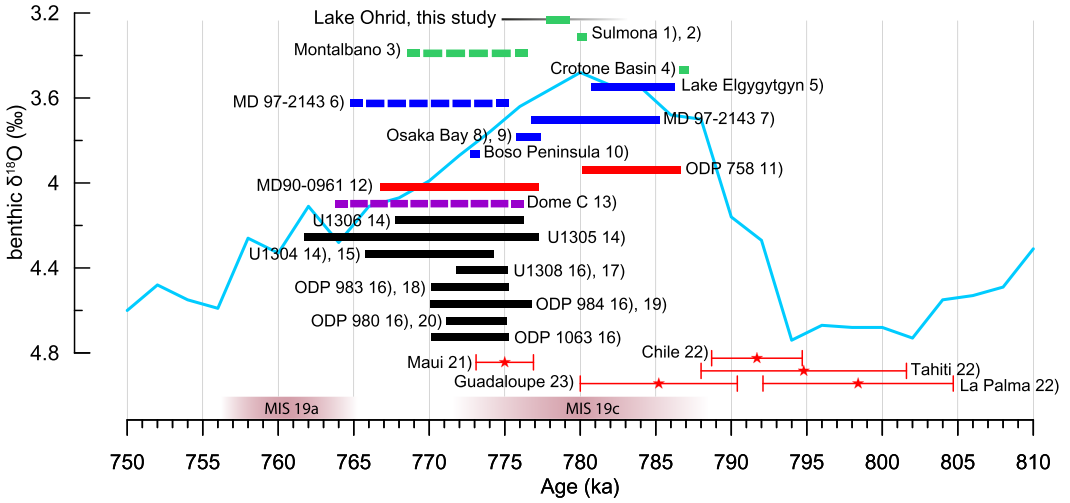

Figure 1. Timing of the Matuyama-Brunhes (MB) reversal plotted with respect to the LR04 benthic $\delta^{18}O$ stack (Lisiecki & Raymo, 2005). Length of bar indicates duration of MB reversal in the various records. Colors relate to geographic regions. Green: Mediterranean, blue: Pacific, red: Indian Ocean, purple: Antarctica, black: North Atlantic. Records utilizing ^{10}Be as a proxy of relative paleointensity (RPI) are indicated by a broken line. For Lake Ohrid the phase of low RPI across the MB is indicated by a shaded bar; note that onset of the RPI minimum cannot be clearly defined because of the presence of greigite (cf. Figure 11). Red stars with error bars: Volcanic ages with uncertainties. (1) Sagnotti et al. (2014), (2) Niespolo et al. (2017), (3) Simon et al. (2017), (4) Macrì et al. (2018), (5) Nowaczyk, Haltia, et al. (2013), (6) Suganuma et al. (2010), (7) Horng et al. (2002), (8) Hyodo et al. (2006), (9) Hyodo and Kitaba (2015), (10) Okada and Niitsuma (1989), (11) Mark et al. (2017), (12) Valet et al. (2014), (13) Dreyfus et al. (2008), (14) Channell (2017a), (15) Xuan et al. (2016), (16) Channell et al. (2010), (17) Channell et al. (2008), (18) Channell and Kleiven (2000), (19) Channell et al. (2004), (20) Channell and Raymo (2003), (21) Coe et al. (2004), (22) Singer et al. (2005), (23) Brown et al. (2013).

the Japan Sea (Hyodo et al., 2006; Hyodo & Kitaba, 2015), while much longer durations are found in sediment cores from the Indian and Atlantic Oceans (Figure 1). Biases of estimated ages in sediments result from uncertainties in the age constraints, unknown lock-in depths, and unknown processes of remanence acquisition (Sagnotti, 2018; Sagnotti et al., 2005; Valet & Fournier, 2016). Moreover, spatial differences in the expression of a reversal may result from nondipolar field configurations during reversals (e.g., Amit et al., 2010; Brown et al., 2007; Leonhardt & Fabian, 2007).

The differences in ages and durations emphasize the uncertainties existing for the geomagnetic reversal processes and the recording in the various types of sediments. A better understanding would enable disentangling phase relationships and teleconnections of paleoclimatic and paleoceanographic changes across different regions and environments. In this study we investigate a composite sediment record from Lake Ohrid (International Continental Scientific Drilling Program ICDP site 5045-1) to precisely date past polarity reversals and understand their internal dynamics. Our sediment composite record is remarkable for various reasons:

It is one of the highest resolved records of the MB boundary with a mean sedimentation rate of 25 cm/kyr.

It has an excellent tephrochronological record of distal volcanic deposits from the Italian volcanic provinces providing a robust independent age control (Leicher et al., 2016, 2019; Wagner et al., 2019).

It has a strongly contrasting climatically controlled sedimentary composition, enabling the development of an orbitally tuned age model.

It is located in the greater Mediterranean region, which has revealed the shortest duration of the MB transition (Macrì et al., 2018; Sagnotti et al., 2014; Sagnotti et al., 2016).

2. Materials

The sediment cores at ICDP "DEEP site" 5045-1 (45°54°N, 38°20°E, 243 m water depth, Figure 2) were retrieved in 2013 in the course of the ICDP project *Scientific Collaboration on past Speciation Conditions in Lake Ohrid* (SCOPSCO; Wagner et al., 2014). A 456 m continuous composite record was constructed

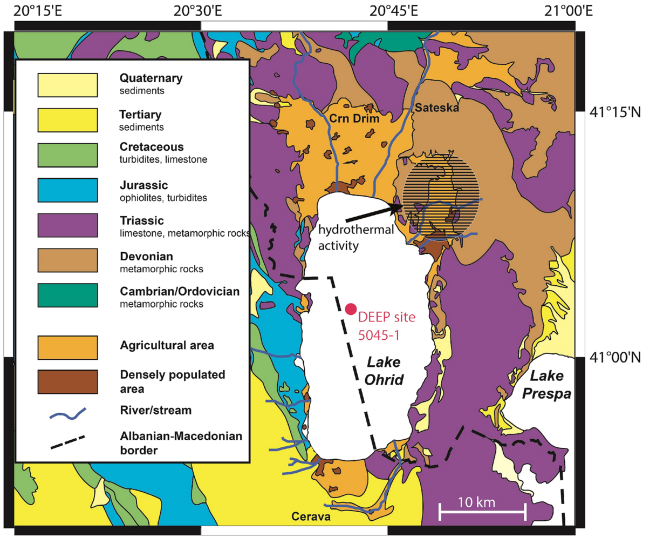

Figure 2. Geologic setting of Lake Ohrid. The DEEP drill site ICDP 5045-1 is shown by the red dot, and an area with hydrothermal activity is indicated by a hatched pattern. Modified after Just et al. (2016) and Vogel et al. (2010).

using the cores recovered from six parallel holes. The upper 448 m are composed of muddy sediments, which vary in composition on glacial-interglacial timescales (Francke et al., 2016; Wagner et al., 2014). Glacial sediments contain a higher proportion of terrigenous material, while an enhanced bioproductivity during interglacials resulted in calcareous, organic matter and diatom-bearing lithologies. Below 447 m composite depth the Lake Ohrid sedimentary record yields shallow lacustrine deposits with intercalated sand-sized layers (Panagiotopoulos et al., 2020), passing downward into a gravelly unit at the bottom of the recovered sequence (Wagner et al., 2014). The age model (supporting information Figure S1; Wagner et al., 2019) is based on tephrostratigraphic correlation of 17 tephra layers (first-order tie points) and a cross-validated orbital tuning approach (second-order tie points). The tuning is based on the rationale that lacustrine productivity is influenced by local summer insolation, while degradation of organic matter is more intense when longer winters promote water column mixing. Thus, minima of total organic carbon in the ICDP 5045-1 record were tuned against inflection points of increasing local summer insolation (moderate lacustrine productivity) and associated increasing winter season length (stronger mixing). We refer to Francke et al. (2016) and Wagner et al. (2019) for details of the tuning process. The obtained age model was additionally evaluated by the paleomagnetic data (this study).

Various investigations have been performed on the younger part of the ICDP 5045-1 core composite, one of which was dedicated to the magnetic mineral content reaching back to 640 ka (247 m). It was found that magnetic mineral assemblages of glacial units experienced modifications by the neoformation of diagenetic Fe minerals (Just et al., 2016). While in the glacial units of MIS 16 to MIS 10 greigite was a typical constituent of the ferrimagnetic mineral assemblage, siderite is commonly found in the glacial units of MIS 8 to MIS 2 (Just et al., 2016; Lacey et al., 2016). The authors hypothesized that greigite formation occurred as an early diagenetic process and the termination of greigite formation after MIS 10 was related to a declining sulfate supply to the lake, giving rise to siderite formation in a methanogenic environment. Throughout the whole composite profile diagenetic Fe minerals were not found within interglacial intervals, which was attributed to a limited availability of reactive iron (Just et al., 2016). Here we discuss the extended rock magnetic data set down to 428 m and the paleomagnetic data acquired on a total of 1,350 samples. Initially, samples were taken at 48 cm increments. A continuous subsampling was conducted across polarity reversals, and additional four off-splice samples were taken across the MB transition for thermal demagnetization.

3. Methods

Magnetic measurements of low-resolution samples (48 cm increment) from the core composite were performed at the Helmholtz Centre Potsdam GFZ, Germany. After this first screening, measurements have been performed on continuously subsampled intervals across detected polarity transitions. The latter samples have been analyzed at the Istituto Nazionale Geofisica e Vulcanologia (INGV) Rome and the Faculty of Geosciences, University of Bremen. Magnetic volume susceptibility (κ) was measured using an AGICO MFK-1A Kappabridge. Measurements of the Natural Remanent Magnetization (NRM) and stepwise alternating field (AF) demagnetization up to 100 mT were carried out using 2G Enterprises cryogenic magnetometers at 10 incremental steps. Afterward an Anhysteretic Remanent Magnetization (ARM) was imparted using a 100 mT AF and 50 μT DC bias field and stepwise demagnetized with a peak field of 100 mT for the high-resolution samples and peak AF of 65 mT for the low-resolution samples.

For the low-resolution samples Isothermal Remanent Magnetization (IRM) was imparted at fields of 1.5 T and a backfield of 200 mT using an external pulse magnetizer, while for the high-resolution samples, the inline long core DC coil of the cryogenic magnetometer at the University of Bremen with a field of 700 mT was used as the maximum field. The magnetization after the highest field step was chosen as the saturation IRM (SIRM). In addition, 60 samples have been selected for detailed IRM acquisition experiments up to

2.7 T (25 incremental steps). Representative IRM acquisition curves were analyzed for coercivity components (Kruiver et al., 2001). Each contributing component to the coercivity spectrum—represented by a log-gauss function—is characterized by its contribution to SIRM (%), the field at which half of the SIRM was reached ($B_{1/2}$), and the width of the curve (dispersion, DP).

Further proxies characteristic for magnetic mineralogy were derived from the basic rock magnetic data. The ratio SIRM/κ has been utilized to discriminate the presence of Fe sulfides, that is, greigite (Fu et al., 2008; Larrasoaña et al., 2007; Nowaczyk et al., 2012; Nowaczyk, Frank, et al., 2013; Reynolds et al., 1994; Roberts et al., 1996) or pyrrhotite (Maher & Thompson, 1999). Fine-grained single-domain particles are prone to ARM acquisition, and thus, the ratio κARM/κ reflects the magnetic grain size in a sample. However, changes in the magnetic mineralogy may compromise the significance of this ratio, as greigite, for example, has on average a higher κARM/κ than magnetite (Peters & Dekkers, 2003). The field at which the magnetization decayed to 50% of its initial value, called the median destructive field (MDF), was derived for both the ARM and NRM demagnetization data and is used as a coercivity proxy. Moreover, we carefully utilize the NRM_{30mT}/ARM_{30mT} as proxy for the relative paleointensity (RPI) in suitable intervals of uniform magnetic mineralogy.

A typical behavior of single-domain (SD) greigite is the acquisition of an artificial magnetization, when subjected to a static three-axes AF demagnetization (Stephenson, 1993). This magnetization is perpendicular to the last AF axis and is called gyroremanent magnetization (GRM). It can be quantified by calculating

$$\Delta GRM/\ \Delta NRM = (FRM-MRM)/(NRM-MRM)$$

whereby FRM is the final magnetization after the demagnetization and MRM is the minimum magnetization reached in the course of the AF demagnetization procedure (Fu et al., 2008).

All directional paleomagnetic data have been analyzed by principal component analysis using Puffinplot (Lurcock & Wilson, 2012) to obtain the Characteristic Remanent Magnetization (ChRM) anchored to the origin and the maximum angular deviation (MAD) was calculated. As cores were not oriented in azimuth and, in addition, were cored by rotary drilling below 160 m, only the inclinations are meaningful. Four samples taken across the MB transition were dried in a μ-Metal shield at room-temperature and afterward impregnated using water glass. The plastic container was carefully removed, and samples have been subjected to thermal demagnetization at 28 temperature steps between room temperature and 600 °C using a Schonstedt oven. Remanences were measured after each step using the cryogenic magnetometer.

Six samples were further characterized by measuring hysteresis loops and First Order Reversal Curves (FORC) at INGV. The hysteresis properties were measured on a MicroMag vibrating sample magnetometer (VSM model 2900, Princeton Measurements Corporation) with a maximum applied field of 1 T. After correcting the slope for paramagnetic contribution (calculated from the slope above 210 mT), the ratio between saturation magnetization and saturation remanence M_{rs}/M_s was calculated. The remanent coercive force B_{cr} was determined from IRM backfield curves, and coercivity B_c was derived from hysteresis loops to compute B_{cr}/B_c. FORC measurements were then carried out on the same specimens. In this study 129 FORCs have been measured for each specimen, in steps of 2.4 mT and an averaging time of 300 ms, using a 1 T saturating field. FORC diagrams (Pike et al., 1999; Roberts et al., 2000) were produced by the FORCinel software developed by Harrison and Feinberg using VARIFORC smoothing (Egli, 2013) with parameters: Sc0 = Scb = 7, Sc1 = Sb1 = 8, λ = 0.1 and first point artifact removed.

Scanning electron microscopy (SEM) was carried out on magnetic extracts, which were obtained by first stirring, later resting a Teflon-covered magnetic finger in suspended sediment slurry, and agitated with NaOP to disintegrate clay aggregates. This process was repeated three to four times, and the magnetic finger was rinsed each time. Afterward water was removed and the last drop of water containing the extracted grains were transferred onto SEM stubs. Further samples from the stratigraphic interval covered by Just et al. (2016) at 176.86 m and 182.14 m depth were prepared by embedding the extract in epoxy resin, and the surface was polished to obtain the internal structure of Fe sulfide mineral aggregates. All SEM analyses comprised imaging of particles using a Quadrant Backscatter Electron Detector (Bruker) at accelerating voltage of 15 kV and energy dispersive spectroscopy (EDS) to obtain the geochemical composition. Quantification of EDS data were conducted using the Quantax Esprit 1.9 software, which utilizes internal libraries to convert energy spectra into relative element concentrations.

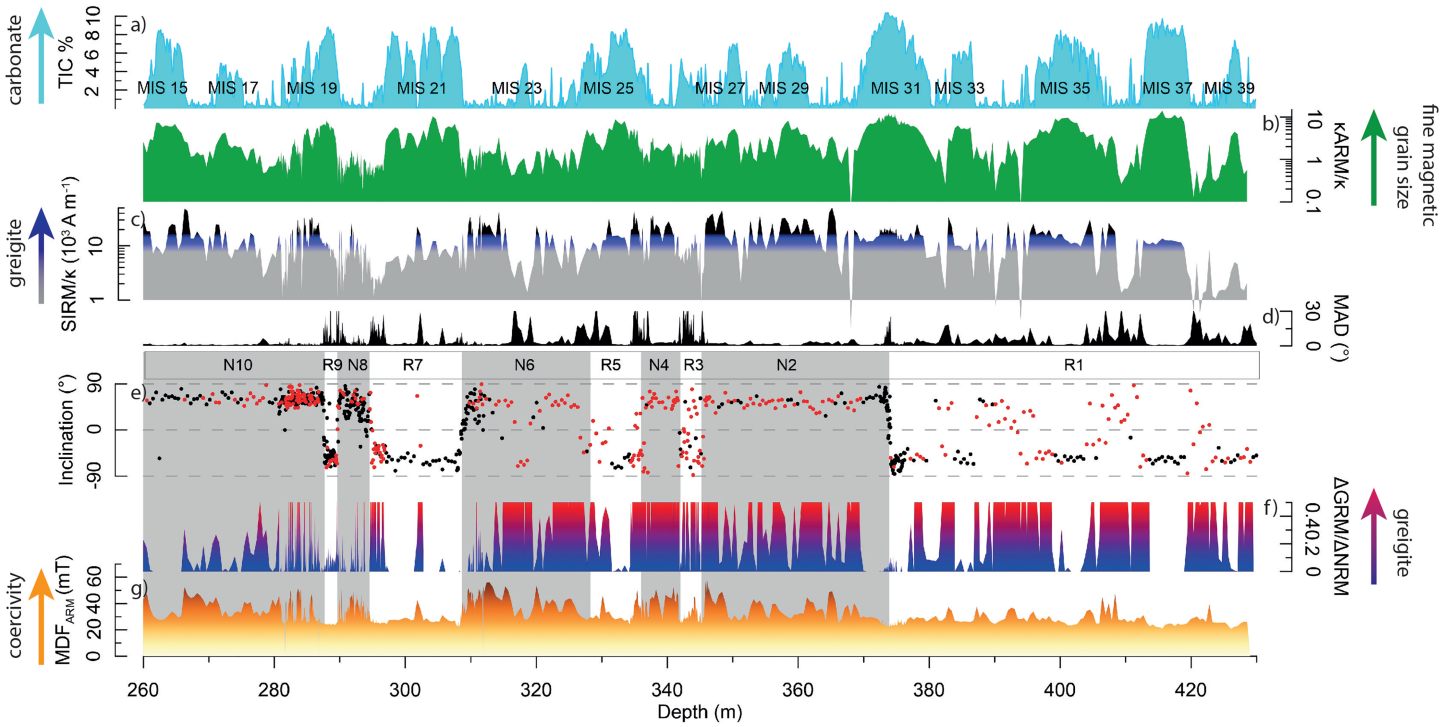

Figure 3. Downcore magnetic parameters of ICDP 5045-1 in relation to (a) ICDP 5045-1 total inorganic carbon (TIC %) with labelled marine isotope stages (MIS), according to the age model. (b) κARM/κ, (c) SIRM/κ, (d) Maximum Angular Deviation (MAD) of (e) inclination of the anchored characteristic remanent magnetization. Inclinations of samples that acquired a significant GRM (ΔGRM/ΔNRM >10%) are shown in red. (f) ΔGRM/ΔNRM, (g) MDF_{ARM}. Where applicable, interpretation of proxies is shown next to axes. Assigned zones of normal (N, gray bars) and reversed (R, white bars) polarity are indicated (see also Table 1).

4. Results

4.1. Variability in Bulk Sediment Composition

The concentration of total inorganic carbon (TIC) varies on glacial-interglacial timescales in Lake Ohrid (Francke et al., 2016; Wagner et al., 2019). Interglacials are characterized by high TIC contents, relating to a higher precipitation and better preservation of in situ produced calcite in the lake and a decrease in terrigenous sediment supply (Francke et al., 2016). The variations in TIC translate to calcium carbonate concentrations between 1–5 weight % for glacial and 50–75 weight % for interglacial intervals. Based on these observations, we plot the TIC variability as a backbone for the further description of glacial-interglacial cyclicity (Figure 3).

Just et al. (2016) presented the magnetic data from the upper part of the sediment record. They observed a general change in the magnetic properties at approximately 150 m depth (350 ka). Above this boundary magnetic concentration proxies show low variability. Below this depth the concentration, mineral assemblage, and granulometry of magnetic minerals show high-amplitude variations on glacial-interglacial timescales.

Glacial-interglacial variability is also the dominant pattern in our newly extended record. The magnetic grain size proxy κARM/κ (Figure 3b) closely resembles TIC % (Figure 3a), with low values (<2.5, coarse grained) during glacials and stadials, indicating an environmental control on the magnetic granulometry and mineralogy. While GRM acquisition (Figure 3f) is solely occurring in glacial and stadial intervals, the greigite proxy SIRM/κ (Figure 3c) shows a more complicated pattern. Below 350 m depth (MIS 26) high SIRM/κ values are found in interglacials, reaching values up to $10*10^3$ A/m, while above high values are associated with glacials and even rise higher than $20*10^3$ A/m. The coercivity proxy MDF_{ARM} (Figure 3g) is in glacial (interglacial) intervals above (below) 30 mT and in some intervals even higher than 40 mT, mimicking changes in SIRM/κ. As for the latter, the high-amplitude glacial variations are muted below 350 m (MIS 26).

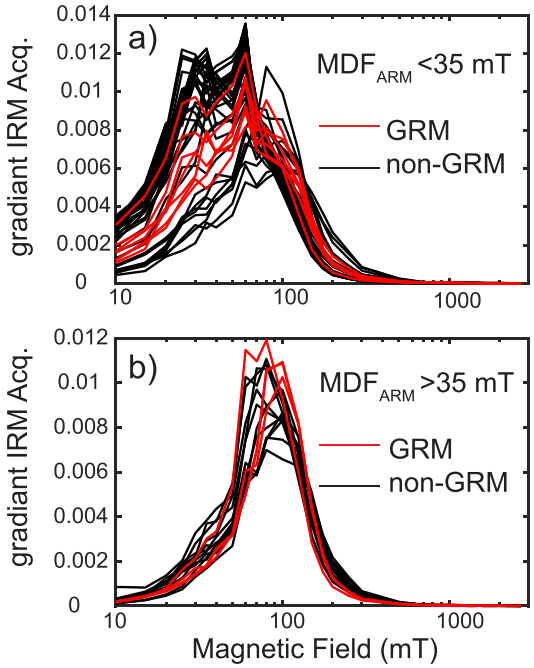

Figure 4. Gradient of Isothermal Remanent Magnetization acquisition for selected samples. (a) In samples with MDF_{ARM} <35 mT the low-coercivity component is strongest expressed by non-GRM samples. GRM samples have stronger contributions of the intermediate component. (b) Samples with MDF_{ARM} >35 mT are dominated by the intermediate coercivity component. See also supporting information Figure S7 and Table S8.

To further disentangle the change in the magnetic mineralogy, we show coercivity distributions of IRM acquisition (Figure 4) separately for samples with high (>35 mT) and low (<35 mT) MDF_{ARM}. Both groups contain samples that acquired a significant GRM upon NRM demagnetization. All samples can be described by three IRM components with $B_{1/2}$ of ~40 mT, ~95 mT, and above 250 mT (Figure 4a and supporting information Figure S7 and Table S8). GRM samples of the MDF_{ARM} <35 mT group have a more emphasized intermediate-coercivity component than non-GRM samples. Samples with MDF_{ARM} >35 mT lack the low-coercivity component and have a suppressed 95 mT component (Figure 4b) and a stronger high-coercivity component.

4.2. Polarity Zones

ChRM was computed for multiple steps, after removal of a viscous overprint at 15 mT AF. Generally, four to seven steps were used; in particular, at polarity transitions the number of steps was adapted to the multiple components of demagnetization vectors. As samples from glacial intervals acquired a GRM at fields higher than 50 mT AF, the initial demagnetization steps could still be utilized to calculate the ChRM. It is important to discriminate between primary post Depositional Remanent Magnetization (pDRM) and secondary Chemical Remanent Magnetizations (CRM), acquired during neoformation of minerals, for example, by greigite (Musgrave & Kars, 2016; Roberts & Rowan, 2005; Sagnotti et al., 2010; Vasiliev et al., 2007). Accordingly, we color coded the inclination data of the samples acquiring a significant GRM (>10% of NRM) in red. To evaluate whether a change in inclination coincides with a mineralogical change, also the coercivity parameter MDF_{ARM} is consulted. The obtained directional data are of good quality with MADs <5° for non-GRM samples and <10° for GRM samples (Figure 3d and 5e). Higher MADs (up to 30°) are restricted to polarity reversals.

In total, 10 polarity zones were defined based on the inclination record (Table 1 and Figure 3) and numbered consecutively. Note that these zones do not necessarily correspond to polarity chrons. As we are interested

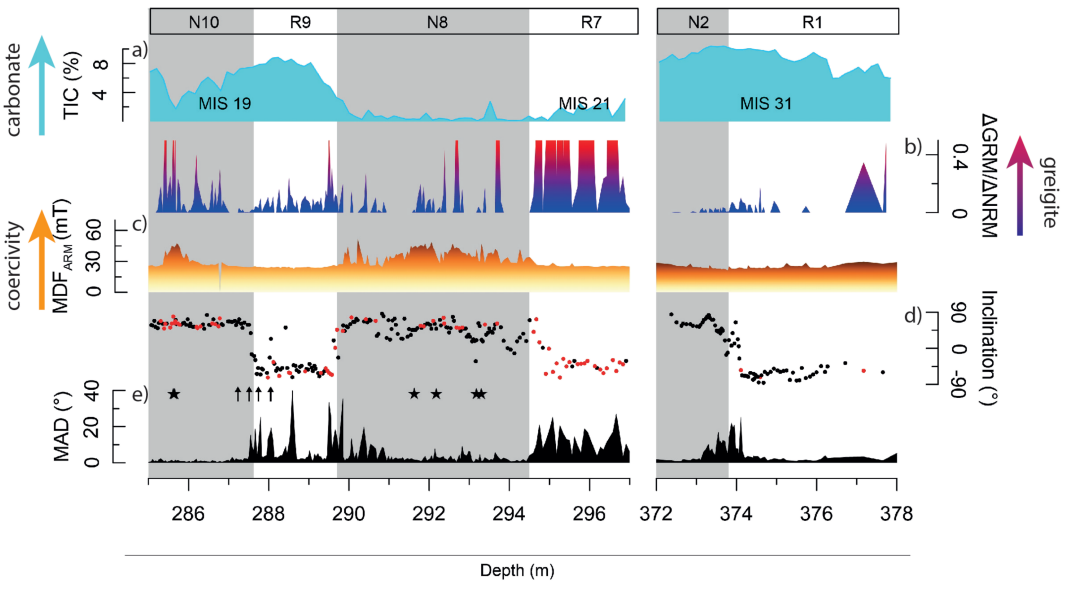

Figure 5. Close-up of MB reversal and base of Jaramillo subchron. Stars mark the position of samples on which FORC measurements were performed (Figure 7 and Table 2). Arrows mark the equivalent composite depths of off-splice samples, which were thermally demagnetized (Figure 6).

Table 1
Polarity Zones of ICDP 5045-1.

Polarity Zone	Top of polarity zone midpoint depth (m)	Top of polarity zone midpoint age (ka)	Thickness of transition (m)	Duration of transition (kyr)	Associated Polarity Chron
N10	0.00	0.0			Brunhes
R9	287.61	778.5	0.20	1.0	Matuyama
N8	289.72	788.3	0.28	1.2	
R7	294.48	806.3	1.56	6.7	
N6	308.75	869.0	1.39	6.0	
R5	328.21	940.1	6.72	17.6	
N4	336.08	961.4	2.50	6.5	
R3	341.93	973.9	0.57	1.2	
N2	345.29	980.5	0.88	1.5	Jaramillo
R1	373.78	1,072.4	0.72	2.3	Matuyama

Note. Depths and ages correspond to midpoints of transitions. Thicknesses and durations indicate the interval of intermediate and unstable directions between polarity zones. Note that polarity zones do not necessarily relate to (sub-) chrons, as they may represent remagnetized intervals. See text for further explanations.

also in the duration of polarity zones, we determine the midpoint and the onset and termination of the polarity transition as follows: We defined the depth, and corresponding age, above which inclinations depart >15° for two consecutive samples as the onset of a polarity transition. The first sample stabilizing at opposite polarity was defined as the termination of the transition. Based on these defined onsets and terminations, the thickness and duration, as well as the midpoint depths and ages of the transitions, were calculated. If not stated otherwise, depths and ages in the text correspond to midpoints of polarity transitions.

Most samples of zone R1 (from the base of the record up to 373.78 m) have reversed polarities, except for a few GRM samples with normal polarities around 423–420 m, 412–405 m, 396–388 m, and 384–381 m composite depth. The transition between R1 and N2 integrates over an interval of 72 cm ($n = 19$) with intermediate directions (Figures 3 and 5). Based on our independent age model (supporting information Figure S1), this transition marks the base of the Jaramillo subchron (Figure 11). Samples at the transition do not show GRM acquisition (Figure 5b), nor does the MDF_{ARM} (Figure 5c) vary, implying an invariable magnetic mineralogy. Zone N2 (373.78–345.29 m) contains both GRM and non-GRM samples of normal polarity. However, all samples in its upper part acquired a GRM.

Above follows a short interval of reversed inclinations (R3, 345.29–341.93 m) revealed by both GRM and non-GRM samples. The following normal polarity zone N4 (341.93–336.08 m) exclusively contains GRM samples. The base coincides with an increase of the MDF_{ARM} up to 45 mT (Figure 5c), which then drops at the top to MDF_{ARM} <30 mT indicating a change of magnetic mineralogy in zone N4. In zone R5 (336.08–328.21 m) MDF_{ARM} remains at values below 35 mT, and GRM and non-GRM samples occur. The transition to zone N6 at 328.21 m is rather thick and integrates over 6.72 m with intermediate inclinations. Normal polarity samples in the lower part of N6 are associated with high MDF_{ARM}. Some GRM samples within N6 (~318 m) have reversed polarity and concurrent drop of the MDF_{ARM}. A rapid drop of the MDF_{ARM} is also observed shortly below the top of N6 at 308.75 m. Except for two samples, zone R7 (308.75–294.48 m) samples did not acquire a GRM and the MDF_{ARM} is low. Again, coinciding change of polarity and coercivity is apparent at the base of zone N8 (294.48–289.72 m). Inclinations in the lower part of N8 are highly variable and sometimes very shallow (Figure 5). Also, in this zone high MDF_{ARM} are not solely attributed to GRM samples, but also, samples showing no GRM acquisition have very high coercivities (also indicated in IRM coercivity distributions in Figure 4b). At the top of this zone the change in coercivity precedes the polarity change: While the MDF_{ARM} already drops below 35 mT at 291 m, the transition to reversed polarity zone R9 only occurs 1.5 m further up in the record and is not accompanied by a systematic change in coercivity. This indicates that mineralogical changes might be responsible for the polarity pattern only in the lower part of zone N8. Zone R9 (289.72–287.61 m) contains GRM and non-GRM samples with MDF_{ARM} <30 mT.

The uppermost polarity boundary (R9-N10) corresponds to the MB reversal with a midpoint depth of 287.61 m. The sample at 287.71 m is the uppermost sample of fully reversed polarity and is followed

by 16 cm ($n = 5$) samples of shallow inclinations and a full recovery of normal polarity at 287.51 m (Figures 5 and 11). Neither a change in MDF_{ARM} nor GRM acquisition is observed at this transition. The inclinations within N10 have stable normal inclinations with a few short-term departures from normal polarity at stratigraphic levels, where excursions would be expected (supporting information Figure S2).

4.3. Thermal Demagnetization

Thermal demagnetization of samples taken from MIS 19 (from a parallel off-splice core), across the transition from R9 to N10 (MB boundary), implies unblocking temperatures of ~180° C (Figure 6), consistent with the presence of (Cr-rich) titanomagnetite grains as remanence carriers (Francombe, 1957) and Al substitution, which are found in our samples (see also section 5.3 and supporting information Figure S4). Unfortunately, the thermally demagnetized samples acquired a random magnetization after heating above ~350 °C, which indicates the formation of magnetite from oxidation of accessible iron. We therefore show thermal demagnetization diagrams up to 300 °C only. The ChRM directions obtained from thermal demagnetization in these temperature steps are in agreement to directions obtained from the AF treated samples from the spliced record. The uppermost samples from 285.23 and 287.51 m have normal polarity. The samples obtained from below the transition (287.74 and 288.05 m) have more noisy demagnetization diagrams. Nevertheless, a normal overprint is clearly visible in AF demagnetized samples, which is removed after the 20 mT AF step. The inclination of the samples from below the MB boundary gets shallower upon heating up to 150 °C. Above this temperature inclinations change sign; however, they remain shallow. This indicates that thermal treatment was not sufficient to remove the normal overprint before forming the new magnetic minerals but still suggests a primary reversed polarity.

4.4. First-Order Reversal Curves

As the concentration of magnetic particles in interglacial samples was too low, hysteresis measurements were noisy, so that FORC measurements were only conducted on samples from glacial intervals (stars in Figure 5). We selected samples from polarity zones N10 (Figures 7a and 7b) and N8 (Figure 7c–7f) with contrasting magnetic proxies (Table 2) that are utilized to infer the presence of greigite. The four samples from N8 are characterized by no or very low GRM acquisition and moderate to low SIRM/κ values, arguing against the presence of greigite, and have relatively coarse magnetic grain size (low to moderate κARM/κ values). In contrast, the two samples from N10 acquired a strong GRM, have high SIRM/κ, and higher κARM/κ (finer magnetic grain size) values and steeper inclinations (Table 2). All selected samples have MDF_{ARM} >35 mT, which is also associated with the dominance of the intermediate-coercivity IRM component (Figure 4).

Except for one, all samples show a concentric distribution in their FORC diagrams, typical for interacting single-domain particles. The concentric contours are offset below the $B_u = 0$ axis, and the maxima are positioned between 60 and 70 mT (B_c), except for a sample at 292.18 m depth, for which it is located below 60 mT. Such closed contours are typical for diagenetic greigite (e.g., Roberts et al., 2011). Moreover, although intensities are relatively low, the lowermost sample (Figure 7f) shows a central ridge, which is often observed for bacterial greigite (Chang et al., 2014; Reinholdsson et al., 2013). Also, in other samples it appears that central ridge may be masked by the concentric contours, but we cannot fully verify this.

There appears to be no systematic differences between GRM and non-GRM samples. However, a slight difference is observed for the lowermost non-GRM samples (Figure 7f), with contours spreading along the B_u axis, which might imply the presence of MD components (Chang et al., 2007; Muxworthy & Roberts, 2007; Roberts et al., 2000), in line with the lowest κARM/κ values. Interestingly, the two lowermost samples have a MDF_{NRM} above 90 mT (Table 2), while the MDF_{ARM} is with ~45 mT comparable to the other samples. This suggests a presence of a high-coercivity phase, which acquired a NRM, but is not prone to ARM acquisition. It could be possible that the high coercivity is related to a diagenetic magnetic phase that acquired a CRM. Hysteresis parameters (Table 2) reveal high B_{cr} (mostly >70 mT) and high M_{rs}/M_s (mostly >0.4) low B_{cr}/B_c (1.35–1.55), which are consistent with the presence of greigite (Chang et al., 2007; Chang et al., 2014; Dekkers & Schoonen, 1996; Peters & Dekkers, 2003; Roberts et al., 2018; Vasiliev et al., 2007) and pyrrhotite (Horng & Roberts, 2006; Roberts et al., 2006). Shallow inclinations observed for these samples (Table 2) may thus result from a diagenetic normal overprint of primary reversed inclinations (cf. section 5.1.3).

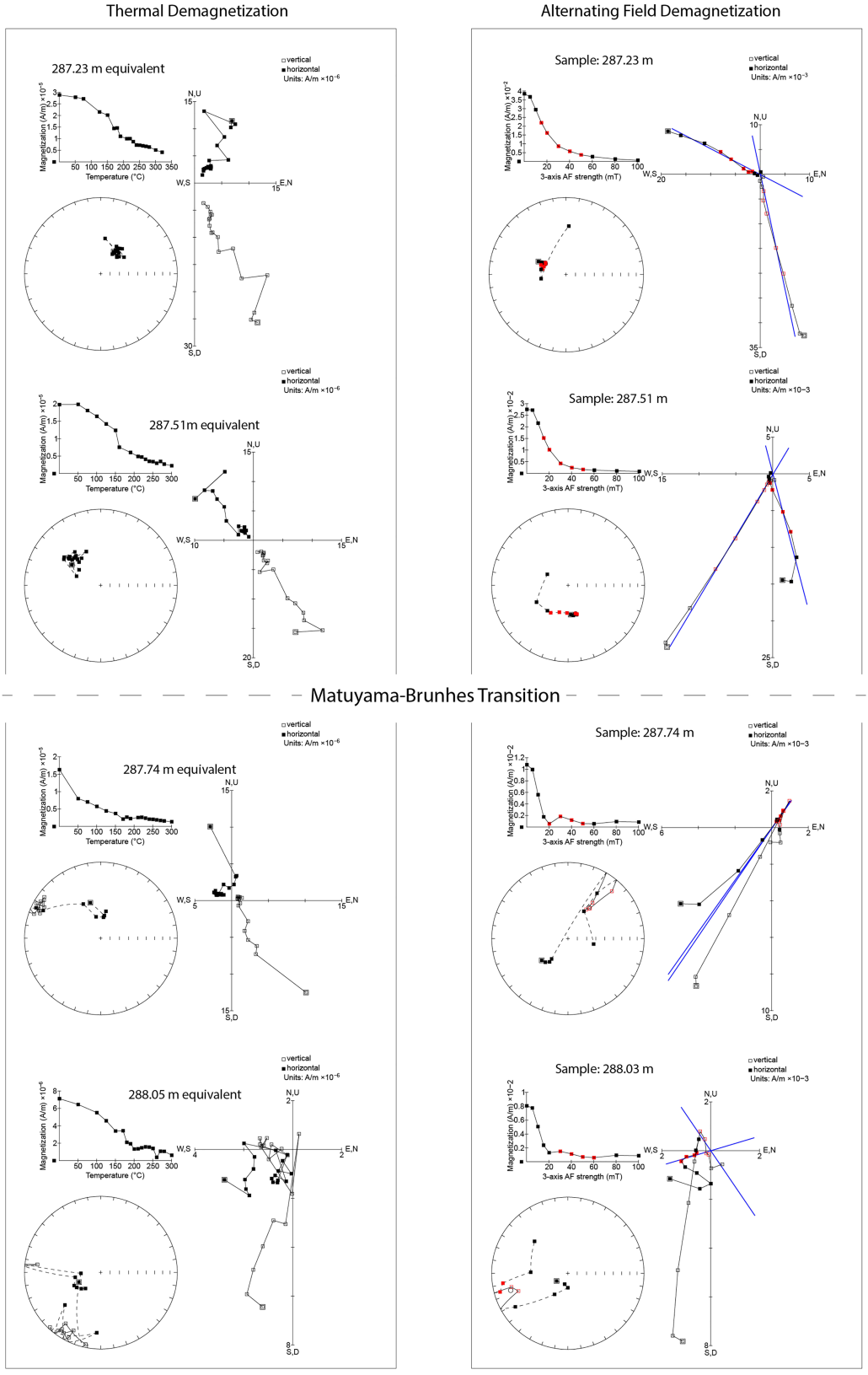

Figure 6. Demagnetization diagrams of samples from above (two upper rows) and below (two lower rows) the MB transition. Left column shows thermal demagnetization data from off-splice samples with indicated equivalent composite depth. Right column shows AF demagnetization data from the core composite. Blue lines indicate anchored ChRM for the AF demagnetized samples.

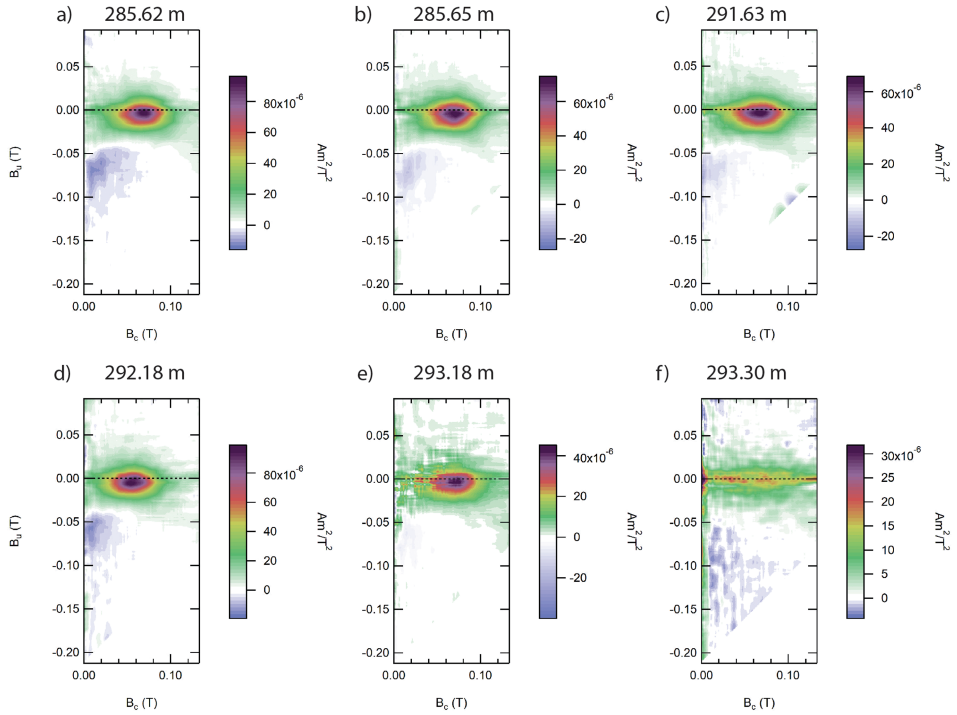

Figure 7. First-order reversal curves of selected samples from (a) 285.62 m, (b) 285.65 m, (c) 291.63 m, (d) 292.18 m, (e) 293.18 m, and (f) 293.30 m. Images were produced using FORCinel (Harrison & Feinberg, 2008) using the VARIFORC smoothing (Egli, 2013) with parameters: Sc0 = Scb = 7, Sc1 = Sb1 = 8, $\lambda = 0.1$. For magnetic properties of samples see Table 2.

5. Discussion

5.1. Reliability of the Paleomagnetic Record

To evaluate the quality of the record for paleomagnetic reconstructions, it is important to understand the process of remanence acquisition, that is, if a magnetization is primary or if the sediments have been remagnetized at a later stage (Hüsing et al., 2009; Jiang et al., 2001; Kelder et al., 2018; Roberts & Rowan, 2005; Sagnotti, 2018; Sagnotti et al., 2010; Vasiliev et al., 2007). According to the coercivity distributions, three components are present in the Lake Ohrid samples (Figure 4). The coercivity distributions of samples with a $MDF_{ARM} < 35$ mT suggest components of 40 mT, 95 mT, and above 250 mT. From this entity, non-GRM samples have the highest contribution of the low-coercivity component, while for the GRM samples the intermediate component has a higher contribution (Figure 4a). We therefore argue that the intermediate-coercivity component is associated with greigite, while the low-coercivity components correspond to detrital magnetite. It should be noted that the coercivity of the greigite component is higher than previously observed for greigite rich samples, which are in the range of $B_{1/2}$ 50–80 mT (Chang et al., 2014; Kelder et al., 2018; Ron et al., 2007; Vasiliev et al., 2007). We will further discuss the reason for the high coercivity

Table 2
Magnetic Properties of Samples Selected for FORC Measurements Shown in Figure 7

Zone	Depth (m)	MDF_{NRM} (mT)	MDF_{ARM} (mT)	MDF_{NRM} / MDF_{ARM}	ARM Incl	κARM/κ	ΔGRM/ΔNRM	SIRM/κ (mA/m)	PCA incl anchored	B_{cr} (mT)	M_{rs}/M_s	B_{cr}/B_c	Figure 7
N10	**285.62**	56.2	44.5	1.26	74	2.15	0.70	24.8	79.3	70	0.51	1.35	7a
N10	**285.65**	55.1	43.5	1.27	82	2.09	0.19	26.0	62.5	71	0.50	1.37	7b
N8	**291.63**	50.6	44.3	1.14	87	1.10	0.02	14.8	46.5	74	0.40	1.54	7c
N8	**292.18**	66.9	36	1.86	88	0.96	0.00	7.2	48.4	63	0.41	1.37	7d
N8	**293.18**	95.4	42.2	2.26	84	0.59	0.00	9.5	20.3	76	0.47	1.43	7e
N8	**293.3**	95.9	46.9	2.04	76	0.53	0.00	7.1	21.4	91	0.27	3.14	7f

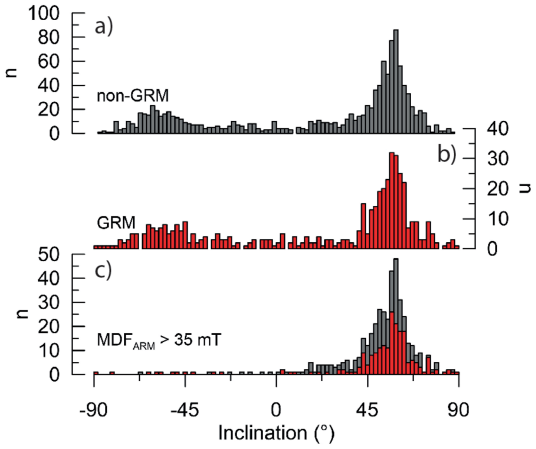

Figure 8. Histograms of inclination plotted for (a) non-GRM samples and (b) GRM samples. (c) Stacked histogram of GRM and non-GRM samples MDF$_{ARM}$ >35 mT.

of this component in section 5.1.3. The presence of the soft components in the interglacial intervals and high κ_{ARM}/κ evidence that low magnetic concentrations are due to carbonate dilution, and not due to dissolution of magnetite.

Turning to the samples having a high MDF$_{ARM}$ (>35 mT), the low-coercivity components are suppressed and the intermediate-coercivity component is dominating (Figure 4b). The different character of theses samples will be used in the following chapter to establish a model for remanence acquisition in our record.

5.1.1. Early Diagenetic Greigite Formation

The first observation in regard of diagenesis is the absence of greigite in the upper 150 m of the composite record (Just et al., 2016), where, instead, siderite is the dominant diagenetic Fe mineral that formed quasi-synsedimentary within the glacial sediments (Lacey et al., 2016). This large-scale change in the diagenetic regime was interpreted to result from changing sulfur availability (Just et al., 2016). A similar control of sulfur presence on the occurrence of greigite has been reported for settings of variable fresh and saline water conditions (Vasiliev et al., 2007). During deposition of the lower unit, in which sulfur was available, the glacial-interglacial variability of greigite is controlled by the concentration of Fe, which is much higher during glacials (Just et al., 2016). They, however, could not answer the question whether the greigite formed in organic matter-rich microenvironments during early diagenesis with sulfur derived from the lake water or during a later stage of diagenesis. The latter option would require an upward diffusion of dissolved sulfur species.

If diagenetic formation of greigite at deeper sediment depth would be a relatively recent process, the inclination of greigite samples should be biased toward normal polarity, compared to non greigite-bearing samples. In Figure 8 we show histograms of inclinations and distinguish between non-GRM (Figure 8a) and GRM (Figure 8b) samples, as this is a common proxy for greigite. The distribution is similar for GRM and non-GRM samples (Figure 8), indicating that greigite carrying a GRM has started to form well in the Matuyama chron.

However, even if the formation of this greigite phase had started already during the Matuyama chron, a formation with a significant time lag after sediment deposition, diachronous recording of a pDRM and CRM would have occurred. In the sediment record this would be archived as a depth lag of polarity switch between samples containing detrital and diagenetic magnetic minerals. Such diachronous recordings are revealed by “ghost reversals” (Musgrave & Kars, 2016). In contrast, an early formation of greigite in shallow sediment depth would result in a reliable magnetostratigraphic record (Kelder et al., 2018; Vasiliev et al., 2007). Below the MB boundary, the uppermost GRM sample of reversed polarity is found at 287.95 m, just 29 cm below the uppermost reversed non-GRM sample (Figure 5). This implies that greigite formation was at least initiated at very shallow burial depth and lags sediment deposition ~1.5 kyr (Figure 11e), according to the orbitally tuned age model. GRM is thus related to early diagenetic greigite.

5.1.2. Late Diagenetic Fe Sulfide Formation

Some samples from glacial intervals with—from a stratigraphic point of view (N4, N6, and N8)—unexpected normal inclinations have MDF$_{ARM}$ values higher than 35 mT, even higher values of MDF$_{NRM}$. They also have B_{cr} higher than 70 mT and elevated SIRM/κ ratios (section 4.1, Figures 3 and 5, and Table 1). The high MDF can be explained by the absence of the low-coercivity component (Figure 4). Thick nodules of Fe sulfides have been described by Just et al. (2016). At the surface of those nodules microcrystalline Fe-S particles with a cubic symmetry are visible (Figure 9a and 9b). Polished thin section reveal that Fe-S particles are embedded in a matrix in the interior part of the nodules (Figure 9c). The nodules's internal structures resemble the amorphous Fe-S rich grains in a matrix found in Pliocene sedimentary rocks in East Timor where they were discussed to be of late diagenetic origin (Aben et al., 2014).

EDS reveal elevated oxygen levels of the nodules. These might relate to oxidation of the sulfide particles after sampling, but elevated oxygen levels might also result from the epoxy resin. Quantified Fe/S ratios vary between 1.3 for the microcrystalline crystals (Figure 9d-1) and 1.6 for the matrix spectra (Figures 9d-2 and

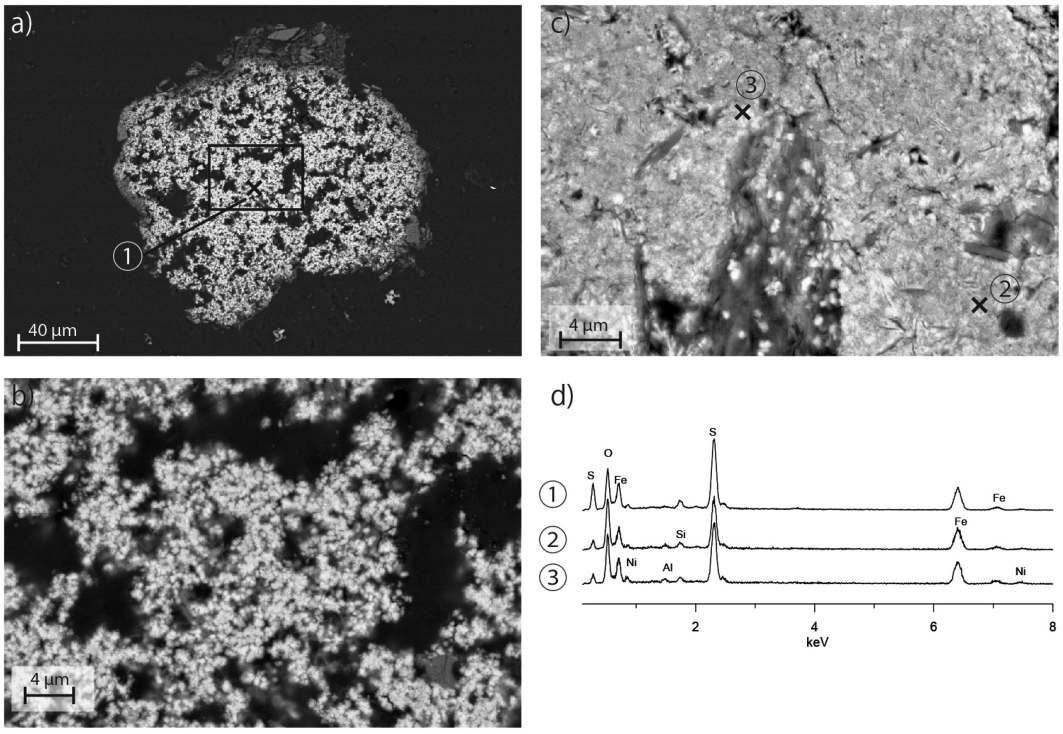

Figure 9. Polished thin sections showing (a) the surface of a Fe sulfide nodule, composed of (b) microcrystalline cubic particles (sample depth 176.86 m). The internal structure of nodules (c) reveals that the crystals are embedded in a fine-grained matrix (sample depth 182.14 m). (d) Energy dispersive spectra (EDS) reveal that the microcrystalline particles have lower Fe/S ratio (1) than the matrix with integrated crystals (2 and 3). See supporting information Table S6 for quantification of EDS.

9d-3). These ratios are much higher than expected for greigite (Fe/S of 0.75). Higher MDFs and coercivities and a higher Fe/S ratio could relate to the presence of pyrrhotite (Dekkers, 1988; Horng & Roberts, 2006; Peters & Dekkers, 2003); however, as summarized by Roberts (2015), pyrrhotite is unlikely to form at an early stage of diagenesis. In any case, the Fe nodules in the ICDP 5045-1 core are much coarser (up to >100 µm) than the sediment matrix, rather arguing for a diagenetic process than for a detrital source. Although the surface of the nodules is often rounded (Just et al., 2016), microcrystalline morphologies (Figures 9a and 9b) resemble cubic symmetries, as would be expected for greigite or pyrite. However, the presence of these nodules in magnetic extracts and the high Fe/S rather argues for greigite than pyrite. We therefore assume that these nodules formed at a later stage during diagenesis and the high Fe/S ratios relate to the oxidation of the greigite particles (Roberts et al., 2011; Rowan & Roberts, 2006). The latter might also explain the very high coercivity of the IRM component (Figure 4) and the high MDF_{ARM} (Roberts et al., 2011; Turner, 2001).

Virtually all samples with MDF_{ARM} higher than 35 mT have normal, often somewhat shallower inclinations (Table 2, skewed distribution in Figure 8c), regardless of GRM acquisition. This suggests that this ferrimagnetic mineral phase formed in greater sediment depth during the Brunhes polarity chron. A late diagenetic formation of Fe sulfides, potentially greigite, requires the advection of additional sulfur species through pore waters. Close to Lake Ohrid sulfur-bearing springs and fumaroles occur, which are related to recent tectonic activities (Hoffmann et al., 2010). We propose that the late diagenetic formation of high-coercivity greigite in the Lake Ohrid sediments was enhanced by migration of sulfidic fluids from below. Also, it is important to stress that these late diagenetic mineral phases only occur in the iron-rich glacial intervals.

The coercivity distributions indicate that greigite has completely masked the primary magnetic assemblage, and the MDF_{ARM} seems to be a suitable proxy to asses this effect. Accordingly, samples with high MDF_{ARM} will be excluded from our magnetostratigraphic reconstruction.

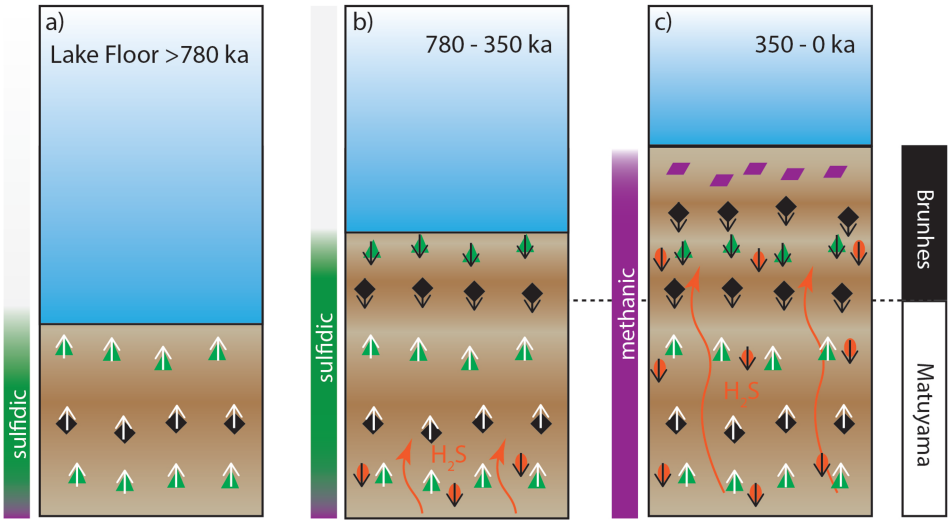

Figure 10. Schematic development of the magnetic mineral assemblage in Lake Ohrid. (a) During the Matuyama chron pore waters were sulfidic and early diagenetic greigite (green triangles, characterized by GRM acquisition) formed in glacial intervals (light brown shadings) at shallow sediment depth, recording the Earth's magnetic field through chemical remanent magnetization (CRM). Interglacial sediments (red brown shadings) were dominated by (titano-)magnetite, which acquired a postdepositional remanent magnetization. (b) These quasi synsedimentary processes continued into the early Brunhes Chron. Additional upward migrating H_2S-rich fluids initiated the growth of a second generation of greigite (orange ellipses, characterized by high MDF) at greater sediment depth. This secondary formation was also dominantly occurring in Fe-rich glacial intervals and led to CRM recording of normal polarity in underlying stratigraphic intervals. (c) During the last 350 ka sulfur availability was reduced and methanogenic conditions prevailed, initiating siderite formation (purple prisms) in shallow sediment depth.

5.1.3. Conceptual Model of Diagenesis in Lake Ohrid

To explain the changing magnetic properties of Lake Ohrid sediments across glacial-interglacial cycles and associated pattern in the paleomagnetic directional record, we developed the following conceptual model (Figure 10). During interglacials the magnetic mineralogy is dominated by detrital low-coercivity (MDF_{ARM} <35 mT, $B_{1/2}$ component 40 mT) (titano-)magnetite grains (black diamonds). Greigite formation (green triangles, GRM acquisition, $B_{1/2}$ component 95 mT) took place at relatively shallow sediment depth in iron rich glacial sediments only (Figure 10a). The formation of greigite almost contemporaneous with magnetite deposition results in a quasi-synchronous recording of the magnetic field through both a CRM and a pDRM, respectively. However, as greigite crystals grew within the whole underlying iron-rich glacial unit, short-lived excursions might be archived as relatively thick intervals of normal polarities (cf. section 5.2).

This early diagenetic formation of greigite persists into the Brunhes Chron (Figure 10b). Moreover, H_2S-rich pore water started to diffuse upward and induced the formation of a second generation of Fe sulfides as coarse nodules (red ellipses, Figure 10b), which are of higher coercivity (high MDF_{ARM}, dominance of $B_{1/2}$ component 95 mT) than the early diagenetic greigite. As the second generation formed during a period of normal polarity, they give rise to anomalous intervals of normal polarity within the Matuyama-aged sediments (Figures 3 and 4, zones N4, N6, and N8). At approximately 350 ka, the geochemical regime of the lake water changed, and instead of greigite, siderite (violet rhomboids, Figure 10c) was the dominant early diagenetic magnetic mineral (Just et al., 2016).

5.2. Potentially Recorded Short-Lived Excursions

When considering the complete downcore record, it emerges that normal polarity samples in N6 and the top of N8 have MDF_{ARM} <35 mT and are not associated with GRM acquisition (Figures 3 and S3). Based on our evaluations, those intervals should not be overprinted by greigite. Interestingly, the top of zone N6 corresponds to the Kamikatsura excursion and the top of N8 falls into the time of the Brunhes precursor (Figure 11). The stratigraphic interval of normal polarity zones N8 and N6, however, is much thicker than the typical duration of excursions, which should be in the order of a few thousand years. The lower parts of zones N8 and N6 are characterized by GRM or high MDF_{ARM} samples, suggesting the presence of

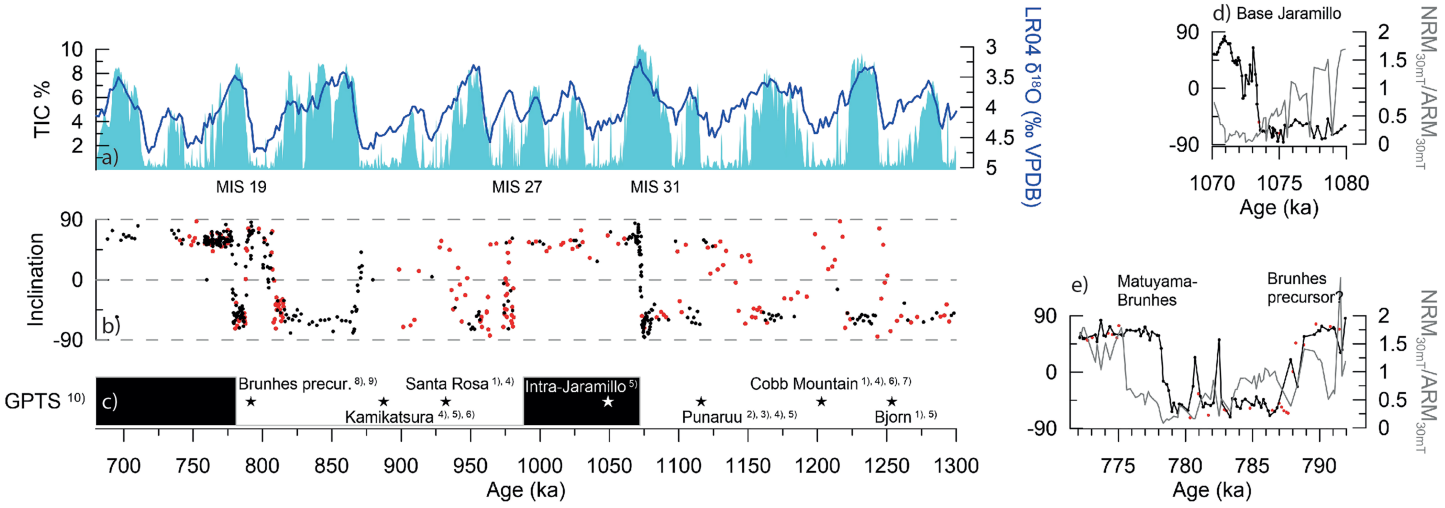

Figure 11. Magnetostratigraphy of ICDP 5045-1. (a) TIC % of ICDP 5045-1 and LR04 (Lisiecki & Raymo, 2005) are shown as a reference for MIS. (b) Cleaned inclination record, only samples with MDF_{ARM} <35 mT are shown. Red: GRM samples, black: non-GRM samples. (c) Geomagnetic Polarity Timescale and geomagnetic excursions: (1) Channell et al. (2002), (2) Channell et al. (2016), (3) Xuan et al. (2016), (4) Singer (2014), (5) Channell (2017b), (6) Panaiotu et al. (2013), (7) Nomade et al. (2005), (8) Singer et al. (2005), (9) Valet et al. (2014), (10) Ogg (2012). (d) Close-up of the base of Jaramillo subchron and (e) Brunhes precursor and MB transition, colors as in (b). The NRM_{30mT}/ARM_{30mT} of non-GRM samples with MDF_{ARM} <35 mT is shown as a proxy for the relative paleointensity.

greigite. Removing the samples with high MDF_{ARM} from our record, the expression of those normal polarity intervals becomes much sharper. It is thus likely that top samples of the respective zones do indeed carry a primary pDRM acquired during the geomagnetic excursions, while in the 1–2 m below the depositional surface contemporaneous greigite formation in the Fe-rich glacial sediments is responsible for ghost remagnetization (Musgrave & Kars, 2016), virtually thickening the reversed sedimentary layer.

Three more intervals of normal polarities within zone R1 and in the lower part of N6 are centered close to the expected Bjorn, Cobb Mountain, and Punaruu and Santa Rosa excursions (Figure 11). The latter intervals are characterized by GRM acquisition, but the MDF_{ARM} is below 35 mT, so that these samples are qualified as containing only early diagenetic greigite. It could thus be possible that these intervals recorded the excursions through an early diagenetic CRM carried by greigite.

5.3. Stratigraphic Position and Timing of Polarity Transitions

The occurrence of greigite in glacial sediments of Lake Ohrid compromised the recording of geomagnetic reversals. The top of the Jaramillo subchron is stratigraphically positioned at the end of glacial MIS 28. In the Lake Ohrid record the top of zone N2 is positioned at 245.29 m, corresponding to 980.5 ka (Table 1). This age is younger than the previously reported GPTS and LR04 age of 988 ka for the top of Jaramillo. In particular, the uppermost samples of zone N2 have MDF_{ARM} exceeding 35 mT, which we interpret as late diagenetic greigite (cf. section 5.1.3). Removing the latter samples, the uppermost normal polarity sample of zone N2 corresponds to an age of 992 ka (Figure 11), closer to the postulated top Jaramillo age. It should be noted, however, that also after cleaning the record by removing the assumed late diagenetic greigite inclinations, the samples of the upper part of N2 all acquired a GRM. Although we assume that the formation of the supposedly early diagenetic greigite had occurred with only a minor time lag after deposition (cf. section 5.1.4) a precise dating of the top Jaramillo subchron is not possible in our record.

The above discussed occurrence of diagenetic minerals is confined to glacial intervals. This is visualized by the absence of GRM and MDF_{ARM} at or below 35 mT in interglacial sections (cf. section 5.1), as well as a clear glacial-interglacial pattern of the $\kappa ARM/\kappa$ (Figure 3b). The bases of the polarity zones N2 and N10 are stratigraphically positioned in MIS 31 and MIS 19 respectively, corresponding to the base of the Jaramillo and to the MB transition (Figure 11). Across these transitions no change in coercivity and magnetic mineralogy is observed. Thermal and alternating field demagnetization diagrams from parallel samples show a consistent polarity pattern, although fully reversed directions were not recovered from the thermal demagnetization diagrams, because of the formation of magnetite upon heating (cf. section 4.3).

Relatively high MADs (~20°) at polarity transitions are attributed to the reversal process. Coarse-grained Fe sulfide nodules, as observed for glacial intervals (Just et al., 2016), were not found in SEM analyses of magnetic extracts from two samples taken from above (287.49 m) and below (287.72 m) the MB transition (supporting information Figure S4). Although few fine-grained Fe sulfide particles were present, magnetite with elevated Cr (18%) and Ni concentrations (8%) and (titano-)magnetite were found to be the dominant constituents of the magnetic fraction. The presence of titanomagnetite and high Cr content magnetite is in line with the thermal demagnetization diagrams, with unblocking temperatures of 180 °C (Francombe, 1957). We consider the magnetic signal in the interglacial sections, namely, MIS 31 and MIS 19, reliable records of the Earth's magnetic field. These polarity transitions can thus be used to date the reversals, as well as to constrain the duration of the base of the Jaramillo and the MB transition.

In the ICDP 5045-1 age model, the midpoint of the base of Jaramillo has an age of 1072 ka (Figure 11d). This age is in line with the GPTS and other published records of the base of the Jaramillo (e.g., Channell et al., 2002; Channell et al., 2010). The transitional phase at the base of Jaramillo integrates over 2.3 kyr.

The MB boundary is stratigraphically placed shortly after peak MIS 19 (778.5 ka, Figures 1, 11e, and S3) only a little younger than its age in the GPTS of 781 ka (Ogg, 2012). However, the midpoint in the Lake Ohrid record is up to 8 kyr older than reported in recently published papers (Figure 1), in which it is located in the younger part of MIS 19 or even close to the MIS 19/MIS 18 boundary (e.g., Channell, 2017a; Suganuma et al., 2010; Valet et al., 2014; Xuan et al., 2016). An absolute comparison of ages can be complicated, as the methods for age model development are different for the different studies. The use of benthic or planktonic foraminifera or other climate relevant parameters from the individual archives on the one hand, and the choice of the dated reference record (e.g., Northern Hemisphere or local insolation and regional or global benthic records), on the other hand, makes age models prone to biases (Valet & Fournier, 2016). Nevertheless, the onset of the MB transition at Lake Ohrid fits relatively well to other records (Figure 1), and it fits to the recently postulated age of 784 ka for the initial collapse of the dipole field (Singer et al., 2019).

The duration of less than 1 kyr for the MB reversal in Lake Ohrid appears much shorter than in other records from most marine archives with durations of typically 5–10 kyr. Such differences cannot be explained by uncertainties in absolute age control. There are also sedimentary archives, which indicate much faster transitions than the 1 kyr at Lake Ohrid. A study of a marine succession outcropping at the Boso peninsula (Japan) from a high sedimentation rate setting (~300 cm/kyr) found the MB transition to last less than 100 years (Okada et al., 2017; Okada & Niitsuma, 1989). A marine succession from the Osaka Bay has likewise a relatively quick reversal of 1 kyr (Hyodo et al., 2006; Hyodo & Kitaba, 2015). Additionally, two sections in Italy revealed a very sharp MB polarity reversal: Macrì et al. (2018) found a duration of less than 100 years in a marine sequence (~50 cm/kyr sedimentation rate) from the Crotone Basin and a duration in the order of few centuries or less was also reported in the Sulmona Basin, in a lacustrine sequence also characterized by high sedimentation rates in the order of 35 cm/kyr (Sagnotti et al., 2014; Sagnotti et al., 2016). The absolute position of the MB reversal in the Sulmona Basin was recently revised (Sagnotti et al., 2018), as it was shown that the precise position of the MB reversal may have been affected by remagnetization (Evans & Muxworthy, 2018; Sagnotti et al., 2018) linked to a cryptotephra, with displacement on the order of centimeters. Regardless of the absolute stratigraphic position, the MB transition in the Sulmona Basin is very rapid (Sagnotti et al., 2018). Finally, a fast MB transition lacking intermediate directions is found in KC-01B core from the Ionian Sea, which has a temporal resolution of 3 kyr (Langereis et al., 1997).

While the proxies for relative paleointensity, that is, NRM_{30mT}/ARM_{30mT}, are strongly biased by the magnetic mineralogical and even more by the remanence acquisition processes (pDRM and CRM), they may provide reliable information for diagenetically unaffected intervals, including the MB transition, in our record (Figure 11e). Interestingly NRM_{30mT}/ARM_{30mT} remains at low values 3 kyr longer than the directional change, which is consistent with the record in Sulmona and closer to the duration of polarity reversals in other records (see Figure 1).

One important factor of the recording process of the Earth's magnetic field is the lock-in zone (Roberts & Winklhofer, 2004; Valet et al., 2016). Under low sedimentation rate settings pDRM acquisition in the lock-in zone would result in a smearing of the transition over a certain depth interval, mostly some tens of centimeters (e.g., Suganuma et al., 2011). The potential to record directional change within a short period of time thus depends on sedimentation rates (Valet et al., 2016). At our site sedimentation rates for this

interval reach up to 23 cm/kyr, which is 2–5 times higher than reported for many marine records (Figure 1). Thus, the smearing of directional change in the lock-in zone in our record is potentially lower and we are able to precisely resolve the spatial and temporal dynamics of the reversal process.

5.4. Implications for Earth's Magnetic Field Reversals

Short durations of reversals are not unlikely, in particular when the dipole moment of the field is lower than the nondipole contributions for a short time as suggested by numerical models (Amit et al., 2010; Brown et al., 2007; Leonhardt & Fabian, 2007). Moreover, directional changes during geomagnetic excursions, which only last some kyrs are likewise very rapid (Leonhardt et al., 2009; Liu et al., 2019; Nowaczyk et al., 2012; Nowaczyk et al., 2018; Roberts & Winklhofer, 2004). Therefore, high-resolution archives are indispensable to reconstruct the internal dynamics of a geomagnetic field during a reversal. Our and other directional records from locations in the Mediterranean region reveal a full polarity switch within a short period of time (Macrì et al., 2018; Sagnotti et al., 2014; Sagnotti et al., 2016). The IMABB4 model—an inversion model based on paleomagnetic data (Leonhardt & Fabian, 2007)—predicts for the MB reversal a low radial magnetic component at the Earth's surface for the Mediterranean region at times when the radial component is still outward (inward) at high latitudes. By that time, the radial component had even already reversed its sign at the core-mantle-boundary (Leonhardt & Fabian, 2007). Interestingly, in IMABBA4 an earlier, and faster polarity switch is also observed for the North Pacific, which fits the reconstruction from Osaka Bay (Hyodo et al., 2006; Hyodo & Kitaba, 2015) and Boso Peninsula (Okada et al., 2017; Okada & Niitsuma, 1989).

Paleomagnetic reconstructions are much sparser for the base of the Jaramillo subchron (Clement & Kent, 1984; Clement & Kent, 1985; Mazaud et al., 2009). A reconstruction of Mazaud et al. (2009) reveals a precursory event with low-latitude Virtual Geomagnetic Pole (VGP) positions and return to higher latitudes before the VGP moves through South America, the Pacific Ocean, and Asia. Such a pattern is consistent with a more complex change of inclination in our record for the base of the Jaramillo (Figure 11d). However, the reversal at Lake Ohrid is also rather quick (ca. 2.3 kyr), while other studies report durations of 5 kyr (Channell et al., 2002). This highlights again that our high-sedimentation site is very suitable to reconstruct the timing and dynamics of reversals.

Leaving the theoretical (oversimplifying) context of VGPs aside, we propose that indeed, nondipolar components of the Earth's magnetic field eventually only dominated for a short period of time in the Mediterranean (Leonhardt & Fabian, 2007) and potentially in the North Pacific, where polarity flips at the MB boundary and at the Base of the Jaramillo occurred suddenly (within 1 and 2.3 kyr, respectively).

5.5. Implications for Magnetostratigraphy

The short decrease of the dipole component of the Earth's magnetic field for the MB reversal and at the base of the Jaramillo subchron is precisely captured in our high sedimentation rate setting. The stratigraphic position of the MB reversal at Lake Ohrid corresponds to the time at which most of the marine records across all ocean basins show the onset of MB transition (Figure 1). Besides smearing within the lock-in zone, local multipolar components of the field after the switch of the dipole component could be responsible for a longer transitional phase in other archives. This inference is in line with the comparable longer phase of low RPI at Lake Ohrid and other archives, while the directional change is much shorter at Lake Ohrid and elsewhere in the Mediterranean. We therefore argue that if the lock-in zone is accounted for or in cases where it may be negligible, as for high sedimentation rate settings (Egli & Zhao, 2015; Roberts & Winklhofer, 2004; Simon et al., 2018; Suganuma et al., 2011), using the onset of the MB transition as a stratigraphic marker is more robust than using the midpoint of the reversal for successfully synchronizing sedimentary archives across the world.

6. Conclusions

The paleomagnetic record from Lake Ohrid is exceptional, as it allows to discriminate the timing of diagenetic mineral neoformation in lacustrine sequences while providing high-resolution records of polarity transitions. Two phases of Fe sulfide formation are evident in the record. Shortly after deposition, greigite formed in shallow sediment depth and acquired a quasi-synsedimentary chemical remanent magnetization. Thus, even in these diagenetically overprinted intervals, reversals and excursions are preserved at the correct

stratigraphic positions, as is evident for the termination of the Jaramillo, the Bjorn Drift, Cobb Mountain, Punarauu, Santa Rosa, and Kamikatsura events. However, the observed stratigraphic intervals of normal polarity at Lake Ohrid correspond to durations, which are much longer than the respective excursions. This can be explained by the formation of early diagenetic greigite within the complete glacial layer in the subsurface. At a later stage of diagenesis, a second greigite phase formed in certain glacial levels throughout the composite record, which is characterized by high coercivity and carries a normal polarity magnetization. We propose that this mineral formed during the Brunhes Chron through precipitation of upward migrating H_2S rich fluids, which are reaching at present the land surface NE of Lake Ohrid.

While we have demonstrated that the magnetic mineralogy in Lake Ohrid sediments is dominated by early and/or late diagenetic Fe sulfides in particular in glacial intervals, the sediments deposited during interglacial phases provide primary records of the Earth's magnetic field based on a detrital magnetization. We date the onset of the MB transition at Lake Ohrid to 778 ka (midpoint age 778.5 ka), with a duration of less than 1 kyr and the transition at the base of the Jaramillo to 1071.3 ka (midpoint age 1072.4 ka) and a duration of about 2.3 kyr. The short durations are preserved because of the high sedimentation rate, which minimizes the smearing of the directional information of the reversal within the lock-in zone. It also emphasizes that the dipole moment was low for only a very short period of time during the reversal. These dipole minima coincide with the phase at which in other archives the onset of the polarity reversal is observed. We advocate that the Mediterranean region is an excellent location to study the temporal development of the dipole field. We further propose that for correlating paleomagnetic records, it is more robust to use the apparent onset of the polarity transition than using its midpoint.

Acknowledgments
We thank Myriam Kars and Liao Chang for very thorough and constructive reviews and additional valuable suggestions by Mark J. Dekkers that helped to improve our manuscript. We acknowledge T. Frederichs and T.v. Dobeneck for fruitful discussions and measurement time at the paleomagnetic laboratory at the University of Bremen. P. Tauber is thanked for providing thin sections of magnetic extracts and P. Witte for SEM analyses. The SCOPSCO Lake Ohrid drilling campaign was funded by the ICDP, the German Ministry of Higher Education and Research, the German Research Foundation, the University of Cologne, the British Geological Survey, the INGV and CNR (both Italy), and the governments of the republics of North Macedonia and Albania. Logistic support was provided by the Hydrobiological Institute in Ohrid. Drilling was carried out by Drilling, Observation and Sampling of the Earth's Continental Crust (DOSECC) and using the Deep Lake Drilling System (DLDS). We thank all collaborators in the SCOPSCO project providing robust (chrono-)stratigraphic framework. Magnetic data of this study are accessible through the Pangaea data repository https://doi.org/10.1594/PANGAEA.908123.

References

Aben, F. M., Dekkers, M. J., Bakker, R. R., van Hinsbergen, D. J. J., Zachariasse, W. J., Tate, G. W., et al. (2014). Untangling inconsistent magnetic polarity records through an integrated rock magnetic analysis: A case study on Neogene sections in East Timor. *Geochemistry, Geophysics, Geosystems*, *15*, 2531–2554. https://doi.org/10.1002/2014GC005294

Amit, H., Leonhardt, R., & Wicht, J. (2010). Polarity reversals from paleomagnetic observations and numerical dynamo simulations. *Space Science Reviews*, *155*(1–4), 293–335.

Brown, M. C., Holme, R., & Bargery, A. (2007). Exploring the influence of the non-dipole field on magnetic records for field reversals and excursions. *Geophysical Journal International*, *168*, 541–550. https://doi.org/10.1111/j.1365-246X.2006.03234.x

Brown, M. C., Jicha, B. R., Singer, B. S., & Shaw, J. (2013). Snapshot of the Matuyama-Brunhes reversal process recorded in $^{40}Ar/^{39}Ar$-dated lavas from Guadeloupe, West Indies. *Geochemistry, Geophysics, Geosystems*, *14*, 4341–4350. https://doi.org/10.1002/ggge.20263

Chang, L., Roberts, A. P., Muxworthy, A. R., Tang, Y., Chen, Q., Rowan, C. J., et al. (2007). Magnetic characteristics of synthetic pseudo-single-domain and multi-domain greigite (Fe_3S_4). *Geophysical Research Letters*, *34*, L24304. https://doi.org/10.1029/2007GL032114

Chang, L., Vasiliev, I., van Baak, C., Krijgsman, W., Dekkers, M. J., Roberts, A. P., et al. (2014). Identification and environmental interpretation of diagenetic and biogenic greigite in sediments: A lesson from the Messinian Black Sea. *Geochemistry, Geophysics, Geosystems*, *15*, 3612–3627. https://doi.org/10.1002/2014GC005411

Channell, J. E. T. (2017a). Complexity in Matuyama–Brunhes polarity transitions from North Atlantic IODP/ODP deep-sea sites. *Earth and Planetary Science Letters*, *467*, 43–56. https://doi.org/10.1016/j.epsl.2017.03.019

Channell, J. E. T. (2017b). Magnetic excursions in the late Matuyama Chron (Olduvai to Matuyama-Brunhes boundary) from North Atlantic IODP sites. *Journal of Geophysical Research: Solid Earth*, *122*, 773–789. https://doi.org/10.1002/2016JB013616

Channell, J. E. T., Curtis, J. H., & Flower, B. P. (2004). The Matuyama–Brunhes boundary interval (500–900 ka) in North Atlantic drift sediments. *Geophysical Journal International*, *158*, 489–505. https://doi.org/10.1111/j.1365-246X.2004.02329.x

Channell, J. E. T., Hodell, D. A., & Curtis, J. H. (2016). Relative paleointensity (RPI) and oxygen isotope stratigraphy at IODP Site U1308: North Atlantic RPI stack for 1.2–2.2 Ma (NARPI-2200) and age of the Olduvai Subchron. *Quaternary Science Reviews*, *131*(Part A), 1–19. https://doi.org/10.1016/j.quascirev.2015.10.011

Channell, J. E. T., Hodell, D. A., Singer, B. S., & Xuan, C. (2010). Reconciling astrochronological and $^{40}Ar/^{39}Ar$ ages for the Matuyama-Brunhes boundary and late Matuyama Chron. *Geochemistry, Geophysics, Geosystems*, *11*, Q0AA12. https://doi.org/10.1029/2010GC003203

Channell, J. E. T., Hodell, D. A., Xuan, C., Mazaud, A., & Stoner, J. S. (2008). Age calibrated relative paleointensity for the last 1.5 Myr at IODP Site U1308 (North Atlantic). *Earth and Planetary Science Letters*, *274*, 59–71. https://doi.org/10.1016/j.epsl.2008.07.005

Channell, J. E. T., & Kleiven, H. F. (2000). Geomagnetic palaeointensities and astrochronological ages for the Matuyama-Brunhes boundary and the boundaries of the Jaramillo Subchron: Palaeomagnetic and oxygen isotope records from ODP Site 983. *Philosophical Transactions of the Royal Society of London, Series A: Mathematical, Physical and Engineering Sciences*, *358*, 1027–1047. https://doi.org/10.1098/rsta.2000.0572

Channell, J. E. T., Mazaud, A., Sullivan, P., Turner, S., & Raymo, M. E. (2002). Geomagnetic excursions and paleointensities in the Matuyama Chron at Ocean Drilling Program Sites 983 and 984 (Iceland Basin). *Journal of Geophysical Research*, *107*(B6), 2114. https://doi.org/10.1029/2001JB000491

Channell, J. E. T., & Raymo, M. E. (2003). Paleomagnetic record at ODP Site 980 (Feni Drift, Rockall) for the past 1.2 Myrs. *Geochemistry, Geophysics, Geosystems*, *4*(4), 1033. https://doi.org/10.1029/2002GC000440

Clement, B. M., & Kent, D. V. (1984). A detailed record of the Lower Jaramillo Polarity Transition from a southern hemisphere, deep-sea sediment core. *Journal of Geophysical Research*, *89*, 1049–1058. https://doi.org/10.1029/JB089iB02p01049

Clement, B. M., & Kent, D. V. (1985). A comparison of two sequential geomagnetic polarity transitions (upper Olduvai and lower Jaramillo) from the Southern Hemisphere. *Physics of the Earth and Planetary Interiors*, *39*, 301–313. https://doi.org/10.1016/0031-9201(85)90144-X

Coe, R. S., Singer, B. S., Pringle, M. S., & Zhao, X. (2004). Matuyama–Brunhes reversal and Kamikatsura event on Maui: Paleomagnetic directions, $^{40}Ar/^{39}Ar$ ages and implications. *Earth and Planetary Science Letters*, *222*, 667–684. https://doi.org/10.1016/j.epsl.2004.03.003

Dekkers, M. J. (1988). Magnetic properties of natural pyrrhotite. Part I: Behaviour of initial susceptibility and saturation-magnetization-related rock-magnetic parameters in a grain-size dependent framework. *Physics of the Earth and Planetary Interiors*, *52*, 376–393. https://doi.org/10.1016/0031-9201(88)90129-X

Dekkers, M. J., & Schoonen, M. A. A. (1996). Magnetic properties of hydrothermally synthesized greigite (Fe_3S_4)—I. Rock magnetic parameters at room temperature. *Geophysical Journal International*, *126*, 360–368. https://doi.org/10.1111/j.1365-246X.1996.tb05296.x

Dreyfus, G. B., Raisbeck, G. M., Parrenin, F., Jouzel, J., Guyodo, Y., Nomade, S., & Mazaud, A. (2008). An ice core perspective on the age of the Matuyama–Brunhes boundary. *Earth and Planetary Science Letters*, *274*, 151–156. https://doi.org/10.1016/j.epsl.2008.07.008

Egli, R. (2013). VARIFORC: An optimized protocol for calculating non-regular first-order reversal curve (FORC) diagrams. *Global and Planetary Change*, *110*, 302–320. https://doi.org/10.1016/j.gloplacha.2013.08.003

Egli, R., & Zhao, X. (2015). Natural remanent magnetization acquisition in bioturbated sediment: General theory and implications for relative paleointensity reconstructions. *Geochemistry, Geophysics, Geosystems*, *16*, 995–1016. https://doi.org/10.1002/2014GC005672

Evans, M. E., & Muxworthy, A. R. (2018). A re-appraisal of the proposed rapid Matuyama–Brunhes geomagnetic reversal in the Sulmona Basin, Italy. *Geophysical Journal International*, *213*, 1744–1750. https://doi.org/10.1093/gji/ggy111

Francke, A., Wagner, B., Just, J., Leicher, N., Gromig, R., Baumgarten, H., et al. (2016). Sedimentological processes and environmental variability at Lake Ohrid (Macedonia, Albania) between 637 ka and the present. *Biogeosciences*, *13*, 1179–1196. https://doi.org/10.5194/bg-13-1179-2016

Francombe, M. H. (1957). Lattice changes in spinel-type iron chromites. *Journal of Physics and Chemistry of Solids*, *3*, 37–43. https://doi.org/10.1016/0022-3697(57)90045-8

Fu, Y., von Dobeneck, T., Franke, C., Heslop, D., & Kasten, S. (2008). Rock magnetic identification and geochemical process models of greigite formation in Quaternary marine sediments from the Gulf of Mexico (IODP Hole U1319A). *Earth and Planetary Science Letters*, *275*, 233–245. https://doi.org/10.1016/j.epsl.2008.07.034

Harrison, R. J., & Feinberg, J. M. (2008). FORCinel: An improved algorithm for calculating first-order reversal curve distributions using locally weighted regression smoothing. *Geochemistry, Geophysics, Geosystems*, *9*, Q05016. https://doi.org/10.1029/2008GC001987

Hoffmann, N., Reicherter, K., Fernández-Steeger, T., & Grützner, C. (2010). Evolution of ancient Lake Ohrid: A tectonic perspective. *Biogeosciences*, *7*, 3377–3386. https://doi.org/10.5194/bg-7-3377-2010

Horng, C.-S., Lee, M.-Y., Palike, H., Wei, K.-Y., Liang, W.-T., Iizuka, Y., & Torii, M. (2002). Astronomically calibrated ages for geomagnetic reversals within the Matuyama chron. *Earth, Planets and Space*, *54*(6), 679–690. https://doi.org/10.1186/BF03351719

Horng, C.-S., & Roberts, A. P. (2006). Authigenic or detrital origin of pyrrhotite in sediments?: Resolving a paleomagnetic conundrum. *Earth and Planetary Science Letters*, *241*, 750–762. https://doi.org/10.1016/j.epsl.2005.11.008

Hüsing, S. K., Dekkers, M. J., Franke, C., & Krijgsman, W. (2009). The Tortonian reference section at Monte dei Corvi (Italy): Evidence for early remanence acquisition in greigite-bearing sediments. *Geophysical Journal International*, *179*, 125–143. https://doi.org/10.1111/j.1365-246X.2009.04301.x

Hyodo, M., Biswas, D. K., Noda, T., Tomioka, N., Mishima, T., Itota, C., & Sato, H. (2006). Millennial- to submillennial-scale features of the Matuyama-Brunhes geomagnetic polarity transition from Osaka Bay, southwestern Japan. *Journal of Geophysical Research*, *111*, B02103. https://doi.org/10.1029/2004JB003584

Hyodo, M., & Kitaba, I. (2015). Timing of the Matuyama–Brunhes geomagnetic reversal: Decoupled thermal maximum and sea-level highstand during Marine Isotope Stage 19. *Quaternary International*, *383*, 136–144. https://doi.org/10.1016/j.quaint.2015.01.052

Jiang, W.-T., Horng, C.-S., Roberts, A. P., & Peacor, D. R. (2001). Contradictory magnetic polarities in sediments and variable timing of neoformation of authigenic greigite. *Earth and Planetary Science Letters*, *193*, 1–12. https://doi.org/10.1016/S0012-821X(01)00497-6

Just, J., Nowaczyk, N. R., Sagnotti, L., Francke, A., Vogel, H., Lacey, J. H., & Wagner, B. (2016). Environmental control on the occurrence of high-coercivity magnetic minerals and formation of iron sulfides in a 640 ka sediment sequence from Lake Ohrid (Balkans). *Biogeosciences*, *13*, 2093–2109. https://doi.org/10.5194/bg-13-2093-2016

Kelder, N. A., Sant, K., Dekkers, M. J., Magyar, I., van Dijk, G. A., Lathouwers, Y. Z., et al. (2018). Paleomagnetism in Lake Pannon: Problems, pitfalls, and progress in using iron sulfides for magnetostratigraphy. *Geochemistry, Geophysics, Geosystems*, *19*, 3405–3429. https://doi.org/10.1029/2018GC007673

Kruiver, P. P., Dekkers, M. J., & Heslop, D. (2001). Quantification of magnetic coercivity components by the analysis of acquisition curves of isothermal remanent magnetisation. *Earth and Planetary Science Letters*, *189*, 269–276. https://doi.org/10.1016/S0012-821X(01)00367-3

Lacey, J. H., Leng, M. J., Francke, A., Sloane, H. J., Milodowski, A., Vogel, H., et al. (2016). Northern Mediterranean climate since the Middle Pleistocene: A 637 ka stable isotope record from Lake Ohrid (Albania/Macedonia). *Biogeosciences*, *13*, 1801–1820. https://doi.org/10.5194/bg-13-1801-2016

Langereis, C. G., Dekkers, M. J., de Lange, G. J., Paterne, M., & van Santvoort, P. J. M. (1997). Magnetostratigraphy and astronomical calibration of the last 1.1 Myr from an eastern Mediterranean piston core and dating of short events in the Brunhes. *Geophysical Journal International*, *129*, 75–94. https://doi.org/10.1111/j.1365-246X.1997.tb00938.x

Larrasoaña, J. C., Roberts, A. P., Musgrave, R. J., Gràcia, E., Piñero, E., Vega, M., & Martínez-Ruiz, F. (2007). Diagenetic formation of greigite and pyrrhotite in gas hydrate marine sedimentary systems. *Earth and Planetary Science Letters*, *261*, 350–366. https://doi.org/10.1016/j.epsl.2007.06.032

Leicher, N., Giaccio, B., Zanchetta, G., Wagner, B., Francke, A., Palladino, D. M., et al. (2019). Central Mediterranean explosive volcanism and tephrochronology during the last 630 ka based on the sediment record from LakeOhrid. *Quaternary Science Reviews*, *226*, 106021. https://doi.org/10.1016/j.quascirev.2019.106021

Leicher, N., Zanchetta, G., Sulpizio, R., Giaccio, B., Wagner, B., Nomade, S., et al. (2016). First tephrostratigraphic results of the DEEP site record from Lake Ohrid (Macedonia and Albania). *Biogeosciences*, *13*, 2151–2178. https://doi.org/10.5194/bg-13-2151-2016

Leonhardt, R., & Fabian, K. (2007). Paleomagnetic reconstruction of the global geomagnetic field evolution during the Matuyama/Brunhes transition: Iterative Bayesian inversion and independent verification. *Earth and Planetary Science Letters*, *253*, 172–195. https://doi.org/10.1016/j.epsl.2006.10.025

Leonhardt, R., Fabian, K., Winklhofer, M., Ferk, A., Laj, C., & Kissel, C. (2009). Geomagnetic field evolution during the Laschamp excursion. *Earth and Planetary Science Letters*, *278*, 87–95. https://doi.org/10.1016/j.epsl.2008.11.028

Lisiecki, L. E., & Raymo, M. E. (2005). A Pliocene-Pleistocene stack of 57 globally distributed benthic $\delta^{18}O$ records. *Paleoceanography*, *20*, PA1003. https://doi.org/10.1029/2004PA001071

Liu, J., Nowaczyk, N., Frank, U., & Arz, H. (2019). Geomagnetic paleosecular variation record spanning from 40 to 20 ka – implications for the Mono Lake excursion from Black Sea sediments. *Earth and Planetary Science Letters*, *509*, 114–124. https://doi.org/10.1016/j.epsl.2018.12.029

Lurcock, P. C., & Wilson, G. S. (2012). PuffinPlot: A versatile, user-friendly program for paleomagnetic analysis. *Geochemistry, Geophysics, Geosystems*, *13*, Q06Z45. https://doi.org/10.1029/2012GC004098

Macrì, P., Capraro, L., Ferretti, P., & Scarponi, D. (2018). A high-resolution record of the Matuyama-Brunhes transition from the Mediterranean region: The Valle di Manche section (Calabria, Southern Italy). *Physics of the Earth and Planetary Interiors*, *278*, 1–15. https://doi.org/10.1016/j.pepi.2018.02.005

Maher, B. A., & Thompson, R. (1999). *Quaternary climates, environments and magnetism*. Cambridge: Cambridge University Press.

Mark, D. F., Renne, P. R., Dymock, R. C., Smith, V. C., Simon, J. I., Morgan, L. E., et al. (2017). High-precision $^{40}Ar/^{39}Ar$ dating of pleistocene tuffs and temporal anchoring of the Matuyama-Brunhes boundary. *Quaternary Geochronology*, *39*, 1–23. https://doi.org/10.1016/j.quageo.2017.01.002

Mazaud, A., Channell, J. E. T., Xuan, C., & Stoner, J. S. (2009). Upper and lower Jaramillo polarity transitions recorded in IODP Expedition 303 North Atlantic sediments: Implications for transitional field geometry. *Physics of the Earth and Planetary Interiors*, *172*, 131–140. https://doi.org/10.1016/j.pepi.2008.08.012

Musgrave, R. J., & Kars, M. (2016). Recognizing magnetostratigraphy in overprinted and altered marine sediments: Challenges and solutions from IODP Site U1437. *Geochemistry, Geophysics, Geosystems*, *17*, 3190–3206. https://doi.org/10.1002/2016GC006386

Muxworthy, A. R., & Roberts, A. P. (2007). First-order reversal curve (FORC) diagrams. In D. Gubbins & E. Herrero-Bervera (Eds.), *Encyclopedia of geomagnetism and paleomagnetism* (pp. 266–272). Dordrecht, The Netherlands: Springer.

Niespolo, E. M., Rutte, D., Deino, A. L., & Renne, P. R. (2017). Intercalibration and age of the Alder Creek sanidine $^{40}Ar/^{39}Ar$ standard. *Quaternary Geochronology*, *39*, 205–213. https://doi.org/10.1016/j.quageo.2016.09.004

Nomade, S., Renne, P. R., Vogel, N., Deino, A. L., Sharp, W. D., Becker, T. A., et al. (2005). Alder Creek sanidine (ACs-2): A Quaternary $^{40}Ar/^{39}Ar$ dating standard tied to the Cobb Mountain geomagnetic event. *Chemical Geology*, *218*, 315–338. https://doi.org/10.1016/j.chemgeo.2005.01.005

Nowaczyk, N. R., Arz, H. W., Frank, U., Kind, J., & Plessen, B. (2012). Dynamics of the Laschamp geomagnetic excursion from Black Sea sediments. *Earth and Planetary Science Letters*, *351–352*, 54–69. https://doi.org/10.1016/j.epsl.2012.06.050

Nowaczyk, N. R., Frank, U., Kind, J., & Arz, H. W. (2013). A high-resolution paleointensity stack of the past 14 to 68 ka from Black Sea sediments. *Earth and Planetary Science Letters*, *384*, 1–16. https://doi.org/10.1016/j.epsl.2013.09.028

Nowaczyk, N. R., Haltia, E. M., Ulbricht, D., Wennrich, V., Sauerbrey, M. A., Rosén, P., et al. (2013). Chronology of Lake El'gygytgyn sediments—A combined magnetostratigraphic, palaeoclimatic and orbital tuning study based on multi-parameter analyses. *Climate of the Past*, *9*, 2413–2432. https://doi.org/10.5194/cp-9-2413-2013

Nowaczyk, N. R., Jiabo, L., Frank, U., & Arz, H. W. (2018). A high-resolution paleosecular variation record from Black Sea sediments indicating fast directional changes associated with low field intensities during Marine Isotope Stage (MIS) 4. *Earth and Planetary Science Letters*, *484*, 15–29. https://doi.org/10.1016/j.epsl.2017.12.009

Ogg, J. G. (2012). Chapter 5—Geomagnetic polarity time scale. In *The Geologic Time Scale* (pp. 85–113). Boston: Elsevier.

Okada, M., & Niitsuma, N. (1989). Detailed paleomagnetic records during the Brunhes-Matuyama geomagnetic reversal, and a direct determination of depth lag for magnetization in marine sediments. *Physics of the Earth and Planetary Interiors*, *56*, 133–150. https://doi.org/10.1016/0031-9201(89)90043-5

Okada, M., Suganuma, Y., Haneda, Y., & Kazaoka, O. (2017). Paleomagnetic direction and paleointensity variations during the Matuyama–Brunhes polarity transition from a marine succession in the Chiba composite section of the Boso Peninsula, central Japan. *Earth, Planets and Space*, *69*(1), 1–19. https://doi.org/10.1186/s40623-017-0627-1

Panagiotopoulos, K., Holtvoeth, J., Kouli, K., Marinova, E., Francke, A., Cvetkoska, A., et al. (2020). Insights into the evolution of the young Lake Ohrid ecosystem and vegetation succession from a southern European refugium during the Early Pleistocene. *Quaternary Science Reviews*. https://doi.org/10.1016/j.quascirev.2019.106044

Panaiotu, C. G., Jicha, B. R., Singer, B. S., Ţugui, A., Seghedi, I., Panaiotu, A. G., & Necula, C. (2013). $^{40}Ar/^{39}Ar$ chronology and paleomagnetism of Quaternary basaltic lavas from the Perşani Mountains (East Carpathians). *Physics of the Earth and Planetary Interiors*, *221*, 1–14. https://doi.org/10.1016/j.pepi.2013.06.007

Peters, C., & Dekkers, M. J. (2003). Selected room temperature magnetic parameters as a function of mineralogy, concentration and grain size. *Physics and Chemistry of the Earth, Parts A/B/C*, *28*, 659–667. https://doi.org/10.1016/s1474-7065(03)00120-7

Pike, C. R., Roberts, A. P., & Verosub, K. L. (1999). Characterizing interactions in fine magnetic particle systems using first order reversal curves. *Journal of Applied Physics*, *85*, 6660–6667. https://doi.org/10.1063/1.370176

Reinholdsson, M., Snowball, I., Zillén, L., Lenz, C., & Conley, D. J. (2013). Magnetic enhancement of Baltic Sea sapropels by greigite magnetofossils. *Earth and Planetary Science Letters*, *366*, 137–150. https://doi.org/10.1016/j.epsl.2013.01.029

Reynolds, R. L., Tuttle, M. L., Rice, C. A., Fishman, N. S., Karachewski, J. A., & Sherman, D. M. (1994). Magnetization and geochemistry of greigite-bearing Cretaceous strata, North Slope basin, Alaska. *American Journal of Science*, *294*, 485–528. https://doi.org/10.2475/ajs.294.4.485

Roberts, A. P. (2015). Magnetic mineral diagenesis. *Earth Science Reviews*, *151*, 1–47. https://doi.org/10.1016/j.earscirev.2015.09.010

Roberts, A. P., Chang, L., Rowan, C. J., Horng, C.-S., & Florindo, F. (2011). Magnetic properties of sedimentary greigite (Fe_3S_4): An update. *Reviews of Geophysics*, *49*, RG1002. https://doi.org/10.1029/2010RG000336

Roberts, A. P., Liu, Q., Rowan, C. J., Chang, L., Carvallo, C., Torrent, J., & Horng, C.-S. (2006). Characterization of hematite (α-Fe_2O_3), goethite (α-FeOOH), greigite (Fe_3S_4), and pyrrhotite (Fe_7S_8) using first-order reversal curve diagrams. *Journal of Geophysical Research*, *111*, B12S35. https://doi.org/10.1029/2006JB004715

Roberts, A. P., Pike, C. R., & Verosub, K. L. (2000). First-order reversal curve diagrams: A new tool for characterizing the magnetic properties of natural samples. *Journal of Geophysical Research*, *105*, 28,461–28,475. https://doi.org/10.1029/2000JB900326

Roberts, A. P., Reynolds, R. L., Verosub, K. L., & Adam, D. P. (1996). Environmental magnetic implications of Greigite (Fe_3S_4) Formation in a 3 m.y. lake sediment record from Butte Valley, northern California. *Geophysical Research Letters*, *23*, 2859–2862. https://doi.org/10.1029/96GL02831

Roberts, A. P., & Rowan, C. J. (2005). Tectonic and geochronological implications of variably timed magnetizations carried by authigenic greigite in marine sediments from New Zealand. *Geology*, *33*, 553–556. https://doi.org/10.1130/g21382.1

Roberts, A. P., Tauxe, L., Heslop, D., Zhao, X., & Jiang, Z. (2018). A critical appraisal of the "Day" diagram. *Journal of Geophysical Research: Solid Earth*, *123*, 2618–2644. https://doi.org/10.1002/2017JB015247

Roberts, A. P., & Winklhofer, M. (2004). Why are geomagnetic excursions not always recorded in sediments? Constraints from post-depositional remanent magnetization lock-in modelling. *Earth and Planetary Science Letters*, *227*, 345–359. https://doi.org/10.1016/j.epsl.2004.07.040

Ron, H., Nowaczyk, N. R., Frank, U., Schwab, M. J., Naumann, R., Striewski, B., & Agnon, A. (2007). Greigite detected as dominating remanence carrier in Late Pleistocene sediments, Lisan formation, from Lake Kinneret (Sea of Galilee), Israel. *Geophysical Journal International*, *170*, 117–131. https://doi.org/10.1111/j.1365-246X.2007.03425.x

Rowan, C. J., & Roberts, A. P. (2006). Magnetite dissolution, diachronous greigite formation, and secondary magnetizations from pyrite oxidation: Unravelling complex magnetizations in Neogene marine sediments from New Zealand. *Earth and Planetary Science Letters*, *241*, 119–137. https://doi.org/10.1016/j.epsl.2005.10.017

Sagnotti, L. (2018). New insights on sediment magnetic remanence acquisition point out complexity of magnetic mineral diagenesis. *Geology*, *46*, 383–384. https://doi.org/10.1130/focus042018.1

Sagnotti, L., Cascella, A., Ciaranfi, N., Macrì, P., Maiorano, P., Marino, M., & Taddeucci, J. (2010). Rock magnetism and palaeomagnetism of the Montalbano Jonico section (Italy): Evidence for late diagenetic growth of greigite and implications for magnetostratigraphy. *Geophysical Journal International*, *180*, 1049–1066. https://doi.org/10.1111/j.1365-246X.2009.04480.x

Sagnotti, L., Giaccio, B., Liddicoat, J. C., Caricchi, C., Nomade, S., & Renne, P. R. (2018). On the reliability of the Matuyama–Brunhes record in the Sulmona Basin—Comment to 'A reappraisal of the proposed rapid Matuyama–Brunhes geomagnetic reversal in the Sulmona Basin, Italy' by Evans and Muxworthy (2018). *Geophysical Journal International*, *216*, 296–301. https://doi.org/10.1093/gji/ggy427

Sagnotti, L., Giaccio, B., Liddicoat, J. C., Nomade, S., Renne, P. R., Scardia, G., & Sprain, C. J. (2016). How fast was the Matuyama–Brunhes geomagnetic reversal? A new subcentennial record from the Sulmona Basin, central Italy. *Geophysical Journal International*, *204*, 798–812. https://doi.org/10.1093/gji/ggv486

Sagnotti, L., Roberts, A. P., Weaver, R., Verosub, K. L., Florindo, F., Pike, C. R., et al. (2005). Apparent magnetic polarity reversals due to remagnetization resulting from late diagenetic growth of greigite from siderite. *Geophysical Journal International*, *160*, 89–100. https://doi.org/10.1111/j.1365-246X.2005.02485.x

Sagnotti, L., Scardia, G., Giaccio, B., Liddicoat, J. C., Nomade, S., Renne, P. R., & Sprain, C. J. (2014). Extremely rapid directional change during Matuyama-Brunhes geomagnetic polarity reversal. *Geophysical Journal International*, *199*, 1110–1124. https://doi.org/10.1093/gji/ggu287

Simon, Q., Bourlès, D. L., Bassinot, F., Nomade, S., Marino, M., Ciaranfi, N., et al. (2017). Authigenic $^{10}Be/^{9}Be$ ratio signature of the Matuyama–Brunhes boundary in the Montalbano Jonico marine succession. *Earth and Planetary Science Letters*, *460*, 255–267. https://doi.org/10.1016/j.epsl.2016.11.052

Simon, Q., Bourlès, D. L., Thouveny, N., Horng, C.-S., Valet, J.-P., Bassinot, F., & Choy, S. (2018). Cosmogenic signature of geomagnetic reversals and excursions from the Réunion event to the Matuyama–Brunhes transition (0.7–2.14 Ma interval). *Earth and Planetary Science Letters*, *482*, 510–524. https://doi.org/10.1016/j.epsl.2017.11.021

Singer, B. S. (2014). A Quaternary geomagnetic instability time scale. *Quaternary Geochronology*, *21*, 29–52. https://doi.org/10.1016/j.quageo.2013.10.003

Singer, B. S., Hoffman, K. A., Coe, R. S., Brown, L. L., Jicha, B. R., Pringle, M. S., & Chauvin, A. (2005). Structural and temporal requirements for geomagnetic field reversal deduced from lava flows. *Nature*, *434*(7033), 633–636. https://doi.org/10.1038/nature03431

Singer, B. S., Jicha, B. R., Mochizuki, N., & Coe, R. S. (2019). Synchronizing volcanic, sedimentary, and ice core records of Earth's last magnetic polarity reversal. *Science Advances*, *5*, eaaw4621. https://doi.org/10.1126/sciadv.aaw4621

Stephenson, A. (1993). Three-axis static alternating field demagnetization of rocks and the identification of natural remanent magnetization, gyroremanent magnetization, and anisotropy. *Journal of Geophysical Research*, *98*, 373–381. https://doi.org/10.1029/92JB01849

Suganuma, Y., Okuno, J.i., Heslop, D., Roberts, A. P., Yamazaki, T., & Yokoyama, Y. (2011). Post-depositional remanent magnetization lock-in for marine sediments deduced from ^{10}Be and paleomagnetic records through the Matuyama–Brunhes boundary. *Earth and Planetary Science Letters*, *311*, 39–52. https://doi.org/10.1016/j.epsl.2011.08.038

Suganuma, Y., Yokoyama, Y., Yamazaki, T., Kawamura, K., Horng, C.-S., & Matsuzaki, H. (2010). ^{10}Be evidence for delayed acquisition of remanent magnetization in marine sediments: Implication for a new age for the Matuyama–Brunhes boundary. *Earth and Planetary Science Letters*, *296*, 443–450. https://doi.org/10.1016/j.epsl.2010.05.031

Turner, G. M. (2001). Toward an understanding of the multicomponent magnetization of uplifted Neogene marine sediments in New Zealand. *Journal of Geophysical Research*, *106*, 6385–6397. https://doi.org/10.1029/2000JB900406

Valet, J.-P., Bassinot, F., Bouilloux, A., Bourlès, D., Nomade, S., Guillou, V., et al. (2014). Geomagnetic, cosmogenic and climatic changes across the last geomagnetic reversal from Equatorial Indian Ocean sediments. *Earth and Planetary Science Letters*, *397*, 67–79. https://doi.org/10.1016/j.epsl.2014.03.053

Valet, J.-P., & Fournier, A. (2016). Deciphering records of geomagnetic reversals. *Reviews of Geophysics*, *54*, 410–446. https://doi.org/10.1002/2015RG000506

Valet, J.-P., Meynadier, L., Simon, Q., & Thouveny, N. (2016). When and why sediments fail to record the geomagnetic field during polarity reversals. *Earth and Planetary Science Letters*, *453*, 96–107. https://doi.org/10.1016/j.epsl.2016.07.055

Vasiliev, I., Dekkers, M. J., Krijgsman, W., Franke, C., Langereis, C. G., & Mullender, T. A. T. (2007). Early diagenetic greigite as a recorder of the palaeomagnetic signal in Miocene–Pliocene sedimentary rocks of the Carpathian foredeep (Romania). *Geophysical Journal International*, *171*, 613–629. https://doi.org/10.1111/j.1365-246X.2007.03560.x

Vogel, H., Wessels, M., Albrecht, C., Stich, H. B., & Wagner, B. (2010). Spatial variability of recent sedimentation in Lake Ohrid (Albania/Macedonia). *Biogeosciences*, *7*, 3333–3342. https://doi.org/10.5194/bg-7-3333-2010

Wagner, B., Vogel, H., Francke, A., Friedrich, T., Donders, T., Lacey, J. H., et al. (2019). Mediterranean winter rainfall in phase with African monsoons during the past 1.36 million years. *Nature*. https://doi.org/10.1038/s41586-019-1529-0

Wagner, B., Wilke, T., Krastel, S., Zanchetta, G., Sulpizio, R., Reicherter, K., et al. (2014). The SCOPSCO drilling project recovers more than 1.2 million years of history from Lake Ohrid. *Scientific Drilling*, *17*, 19–29. https://doi.org/10.5194/sd-17-19-2014

Xuan, C., Channell, J. E. T., & Hodell, D. A. (2016). Quaternary magnetic and oxygen isotope stratigraphy in diatom-rich sediments of the southern Gardar Drift (IODP Site U1304, North Atlantic). *Quaternary Science Reviews*, *142*, 74–89. https://doi.org/10.1016/j.quascirev.2016.04.010